bioRxiv preprint doi: https://doi.org/10.1101/2023.10.10.561757; this version posted October 13, 2023. The copyright holder for this preprint (which was not certified by peer review) is the author/funder, who has granted bioRxiv a license to display the preprint in perpetuity. It is made available under aCC-BY-NC-ND 4.0 International license.

Mapping the topography of spatial gene expression with interpretable deep learning

Uthsav Chitra[1], Brian J. Arnold[1,2], Hirak Sarkar[1,3], Cong Ma[1], Sereno Lopez-Darwin[4], Kohei Sanno[1,2], and Benjamin J. Raphael[*1]

[1]Department of Computer Science, Princeton University, Princeton, NJ, USA
[2]Center for Statistics and Machine Learning, Princeton University, Princeton, NJ, USA
[3]Ludwig Cancer Institute, Princeton Branch, Princeton University, Princeton, NJ, USA
[4]Lewis-Sigler Institute, Princeton University, Princeton, NJ, USA

Abstract

Spatially resolved transcriptomics technologies provide high-throughput measurements of gene expression in a tissue slice, but the sparsity of this data complicates the analysis of spatial gene expression patterns such as gene expression gradients. We address these issues by deriving a *topographic map* of a tissue slice—analogous to a map of elevation in a landscape—using a novel quantity called the *isodepth*. Contours of constant isodepth enclose spatial domains with distinct cell type composition, while gradients of the isodepth indicate spatial directions of maximum change in gene expression. We develop GASTON, an unsupervised and interpretable deep learning algorithm that simultaneously learns the isodepth, spatial gene expression gradients, and piecewise linear functions of the isodepth that model both continuous gradients and discontinuous spatial variation in the expression of individual genes. We validate GASTON by showing that it accurately identifies spatial domains and marker genes across several biological systems. In SRT data from the brain, GASTON reveals gradients of neuronal differentiation and firing, and in SRT data from a tumor sample, GASTON infers gradients of metabolic activity and epithelial-mesenchymal transition (EMT)-related gene expression in the tumor microenvironment.

[*]Correspondence: braphael@princeton.edu

bioRxiv preprint doi: https://doi.org/10.1101/2023.10.10.561757; this version posted October 13, 2023. The copyright holder for this preprint (which was not certified by peer review) is the author/funder, who has granted bioRxiv a license to display the preprint in perpetuity. It is made available under aCC-BY-NC-ND 4.0 International license.

1 Introduction

Gene expression varies substantially across a tissue, due to both the spatial organization of cell types within a tissue and localized changes in cell state through processes such as development, differentiation, and intercellular communication [160]. Many genes display sharp, discontinuous changes in expression in certain areas of a tissue, often near the boundaries of distinct *spatial domains* containing different combinations of cell types. For example, different cortical and neocortical layers of the brain are distinguished by the presence and absence of expression of certain marker genes [124, 96]. Gene expression may also vary *continuously* in a tissue, forming gene expression *"gradients"* that distinguish different cell types or states and drive fundamental biological processes including development [6, 55, 48, 117] and cellular communication [148, 138]. For instance, gene expression gradients underlie the functional heterogeneity of neurons in the hippocampus [160, 21] and hepatocytes in individual liver lobules [9, 25]. In tumors, gene expression may vary continuously with the distance to the surrounding stroma due to oxygen gradients or cellular interactions [125, 12].

Spatially resolved transcriptomics (SRT) technologies produce high-throughput measurements of spatial gene expression, quantifying the number of RNA transcripts at thousands in a tissue slice [93, 88, 101, 111, 134, 139]. These SRT technologies enable the inference of spatial domains in tissues as well as the identification of genes and cell types with continuous and discontinuous spatial patterns of expression within and across spatial domains. However, SRT technologies typically yield sparse measurements of the transcriptome: current whole-transcriptome sequencing-based technologies [1, 116, 127, 22, 78] have limited coverage ($\approx$ 500-5,000 unique molecular identifiers (UMIs) per location) while imaging-based technologies measure a much smaller and targeted panel of transcripts (typically 100-1,000 transcripts) [61, 143, 162, 91, 52]. This sparsity markedly complicates the analysis of spatial gene expression.

Numerous computational approaches have been developed to identify spatial domains and/or genes with spatially varying expression from SRT data. These methods typically leverage correlations between expression measurements at nearby spatial locations to overcome the sparse measurements at individual locations. Many methods focus on the identification of distinct spatial domains by partitioning tissues into subregions having large, discontinuous changes in gene expression, e.g. [168, 58, 32, 104, 81, 153, 76, 167, 53], but do not model continuous gene expression gradients within these regions. Several other methods instead test whether the expression of an individual gene varies spatially by fitting a function to the observed transcript counts at spatial locations [132, 130, 171, 18, 145]. However, these methods cannot distinguish continuous gradients within spatial domains from discontinuous changes in expression between domains. More generally, neither approach models the geometry of a tissue slice using a coordinate system that describes both the boundaries of spatial domains and the *relative* position of spatial locations within these domains, thus greatly limiting their ability to identify continuous gradients of gene expression.

We introduce *gene expression topography*, a fundamentally different approach to modeling spatial variation in gene expression. We derive a *"topographic map"* of a tissue slice using the *isodepth*, a 1-dimensional coordinate over the tissue slice which describes both the arrangement of spatial domains and the relative position of each spatial location within its corresponding spatial domain. Thus, just as the topographic map of a landscape demarcates mountains and valleys by their elevation, our topographic map of gene expression delineates spatial domains by their isodepth. Moreover, like the elevation of a landscape, the isodepth varies continuously over a tissue slice, providing a coordinate to model continuous variation in the expression of individual genes. In particular, our topographic map describes *gene expression gradients*, similar to how a topographic map of elevation shows whether a direction is a steep ascent or a flat plateau.

We develop Gradient Analysis of Spatial Transcriptomics Organization with Neural networks (GASTON), an unsupervised and interpretable deep neural network algorithm that learns the isodepth of a tissue slice, the vector field of spatial gradients of gene expression, and spatial expression functions for individual genes directly from SRT data. In particular, GASTON models gene expression as a *piecewise linear* function of

bioRxiv preprint doi: https://doi.org/10.1101/2023.10.10.561757; this version posted October 13, 2023. The copyright holder for this preprint (which was not certified by peer review) is the author/funder, who has granted bioRxiv a license to display the preprint in perpetuity. It is made available under aCC-BY-NC-ND 4.0 International license.

the isodepth, thus describing both continuous gradients and sharp discontinuities in gene expression. We demonstrate that the isodepth and spatial gradients learned by GASTON reveal the geometry and continuous gene expression gradients of multiple tissues across multiple SRT technologies including 10x Genomics Visium [1], Slide-SeqV2 [116, 127], and Stereo-Seq [22]. On SRT data from the mouse and human brain, we show that GASTON more accurately identifies spatial domains and marker genes compared to existing methods, derives maps of spatial variation in cell type organization, and uncovers spatial gradients of neuronal firing and differentiation. Using SRT data from a colorectal tumor sample, we demonstrate that GASTON identifies gradients of metabolic activity in the tumor interior, and gradients of epithelial-mesenchymal transition (EMT)-related gene expression at the tumor-stroma boundary.

2 Results

2.1 GASTON learns the topography of a tissue slice using interpretable deep learning

We introduce the *isodepth* d, a scalar quantity that models the *"topography"* of a tissue slice and is analogous to the elevation in a topographic map of a land surface. A small number of contours of equal isodepth d partition the tissue slice into spatial domains, while the intermediate isodepth contours define the relative position of a location within a domain. Moreover, the gradient ∇d of the isodepth d at each location describes the *spatial gradient*, or the direction of maximum change in gene expression within each spatial domain. The collection of spatial gradients defines a spatial transcriptomic vector field $\mathbf{v}(x, y)$ across the tissue slice T (Figure 1A). Thus, the isodepth describes the *geometry* of a tissue slice, i.e. the arrangement of distinct spatial domains in the tissue, as well as directions of continuous variation within each spatial domain (Methods).

To learn the isodepth d from spatially resolved transcriptomics (SRT) data, we develop Gradient Analysis of Spatial Transcriptomics Organization with Neural networks (GASTON). GASTON models the expression $f_g(x, y)$ of each gene g at spatial location (x, y) as a *piecewise linear* function of the isodepth $d(x, y)$:

$$f_g(x, y) = \sum_{p=1}^{P} (\alpha_{p,g} + \beta_{p,g} \cdot d(x, y)) \cdot 1_{\{(x,y) \in R_p\}}, \tag{1}$$

where the pieces $R_1, \ldots, R_P$ are spatial domains, and $\alpha_{p,g}$ and $\beta_{p,g}$ are the y-intercept and slope, respectively, in the pth spatial domain R_p. We use piecewise linear functions as they are a simple class of models that incorporates both continuous variation in gene expression within each domain, i.e. "gradients" of expression, while allowing for discontinuities in expression at the boundaries of the spatial domains. The boundaries of each spatial domain R_p are given by contours of equal isodepth $d(x, y)$ (Methods). We emphasize that our model does not restrict the spatial domains R_p to be contiguous regions; thus, GASTON is able to model *long-range* spatial correlations in gene expression [101], in contrast to many existing approaches that only model local spatial correlations (Methods).

GASTON jointly learns the isodepth d and piecewise linear gene expression functions f_g in a completely unsupervised manner using an interpretable deep learning model. Specifically, GASTON trains a neural network to learn a composite function $f \circ d(x, y)$ from spatial coordinates to gene expression features, where the isodepth $d(x, y)$ corresponds to an interpretable hidden layer of the network (Figure 1B). GASTON then uses segmented regression [83, 3, 7] to learn the spatial domains R_p, as well as the parameters α, β of the piecewise linear expression functions f_g for each gene g. We demonstrate below that GASTON's interpretable approach uncovers meaningful spatial domains (Figure 1C), and continuous gradients and discontinuities in gene expression (Figure 1D) and cell type composition (Figure 1E) across a wide range of SRT technologies and biological systems including the brain and the tumor microenvironment (Figure 1F).

bioRxiv preprint doi: https://doi.org/10.1101/2023.10.10.561757; this version posted October 13, 2023. The copyright holder for this preprint (which was not certified by peer review) is the author/funder, who has granted bioRxiv a license to display the preprint in perpetuity. It is made available under aCC-BY-NC-ND 4.0 International license.

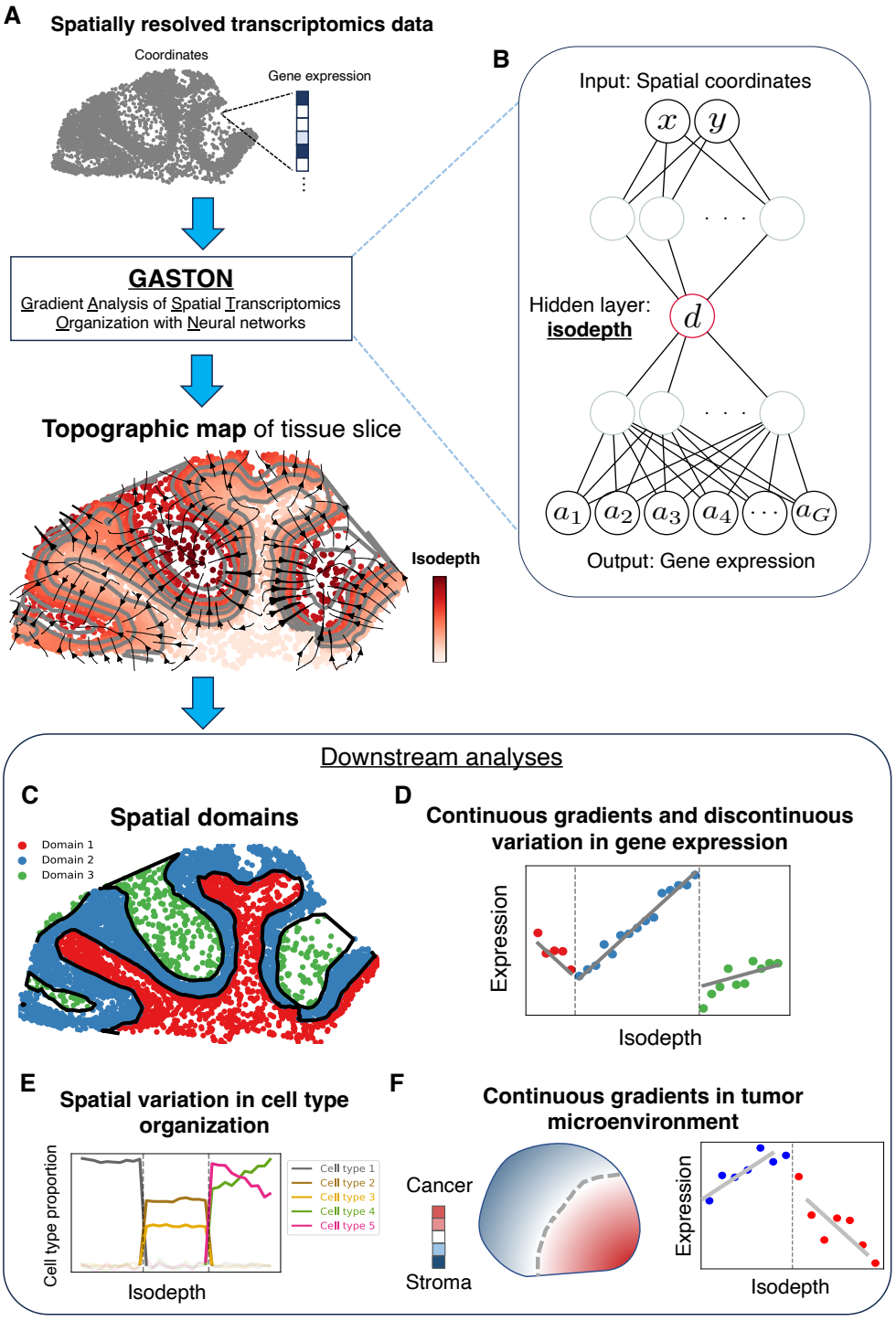

Figure 1: **GASTON, an interpretable deep neural network, learns the topography of a tissue. (A)** GASTON takes in spatially resolved transcriptomics (SRT) data from a tissue slice and outputs the *isodepth*, a coordinate describing a *topographic map* of the tissue slice, with contours of constant isodepth in gray and spatial gradients shown as streamlines. **(B)** GASTON trains a deep neural network to predict gene expression from spatial coordinates, where the isodepth is the value of an *interpretable* hidden layer of the trained neural network. The isodepth learned by GASTON enables many downstream tasks including: **(C)** identification of *spatial domains*, or tissue regions characterized by different cell type composition and gene expression patterns; **(D)** identification of genes with continuous gradients and/or discontinuous variation in expression as a function of isodepth; **(E)** modeling of variation in cell type composition as a function of isodepth; and **(F)** analysis of continuous gene expression gradients in the tumor microenvironment.

bioRxiv preprint doi: https://doi.org/10.1101/2023.10.10.561757; this version posted October 13, 2023. The copyright holder for this preprint (which was not certified by peer review) is the author/funder, who has granted bioRxiv a license to display the preprint in perpetuity. It is made available under aCC-BY-NC-ND 4.0 International license.

2.2 GASTON recapitulates spatial organization in mouse and human brain slices

We first used GASTON to learn the isodepth d and the spatial gradients ∇d in a tissue slice from the mouse cerebellum where the expression of 23,096 transcripts at 9,985 spatial locations was measured using the Slide-SeqV2 platform [116, 127]. The learned isodepth d provides a "topographical map" of the layered geometry of the cerebellum, including the boundaries of distinct layers of the cerebellum, with the depth within each layer scaled to approximate μm (Figure 2A, Methods). The spatial expression gradients ∇d are perpendicular to the cerebellar layers (contours of constant isodepth) and indicate the spatial direction of maximum change in gene expression.

GASTON divides the tissue into four contiguous spatial domains, which are visually consistent with the four distinct layers of the cerebellum – the oligodendrocyte layer, the granular layer, the Purkinje-Bergmann layer, and the molecular layer – that were identified in prior imaging studies [116, 26] and SRT analyses [116, 19, 18] (Figure 2B). We compared the spatial domains learned by GASTON to those identified by Non-negative Spatial Factorization (NSF) [135], SpaGCN [58], and SpiceMix [24] (Figure 2C-E), three recent methods that showcase the major approaches currently used to model local spatial correlations in spatial transcriptomics data: Gaussian processes (GPs), graph convolutional networks (GCNs), and hidden Markov random fields (HMRFs), respectively. We observed that GASTON's spatial domains have much larger spatial coherence [159] compared to the other methods (Figure 2F), showing that the domains identified by GASTON better align with the structured geometry of the cerebellum [140]. Next, we compared the spatial domains to the cell types reported in the original publication of the data (Figure 2G). These cell types were obtained from RCTD [19], a method which performs cell type deconvolution using a reference scRNA-seq dataset and does not take spatial information into account. The GASTON, SpaGCN, and NSF spatial domains have similar agreement with the cell types inferred by RCTD and with each other, while the SpiceMix spatial domains have low agreement with the RCTD cell types and the other methods (Figure 2H). These results demonstrate that the global model of spatial variation used in GASTON identifies more spatially coherent spatial domains than existing methods while still preserving cell type information.

A key distinguishing feature of GASTON is that it learns the isodepth d, which provides a coordinate to analyze the continuous variation in cell types within and across the layers of the cerebellum. Such continuous variation is not modeled by the three methods above nor by the numerous other methods that divide a tissue slice into spatial domains, e.g. [168, 32]. We find that the proportion of cell types varies considerably as a function of the isodepth (Figure 2I). First, we observe that oligodendrocytes and granule cells have large and nearly constant proportion throughout the range of isodepth d that corresponds to the named layers. Moreover, there is a sharp transition in proportion at the isodepth value that GASTON marks as the boundary between these layers, indicating that the learned isodepth d and spatial domains are accurately separating the oligodendrocyte and granule layers.

In contrast, the proportion of Purkinje cells and Bergmann glia exhibit spatial variation with the Purkinje-Bergmann layer. Purkinje cells are concentrated at the start of the layer (small isodepth), while the Bergmann glia peak in proportion inside the layer and are present over a wider range of isodepths (Figure 2J). These results agree with prior imaging and microscopy-based studies which show that Purkinje cells form a "monolayer" in the cerebellum, i.e. a layer with single-cell depth [170, 126, 13] while the Bergmann glia do not form a monolayer but are more diffusely spread out across the Purkinje-Bergmann layer [5, 72]. Interestingly, previous studies have found that the Bergmann glia form a monolayer during the development of the cerebellum [68, 54], and thus the observed arrangement of Bergmann glia here could indicate that the spatial arrangement of Bergmann glia changes after development. We also observe that the Bergmann glia are closer to the molecular layer of the cerebellum compared to Purkinje cells, which agrees with previous studies on cerebellar organization [115].

We emphasize that GASTON learns the isodepth *de novo* and in an unsupervised manner. In contrast, existing approaches for learning depth or depth-like measurements either require prior anatomical knowl-

bioRxiv preprint doi: https://doi.org/10.1101/2023.10.10.561757; this version posted October 13, 2023. The copyright holder for this preprint (which was not certified by peer review) is the author/funder, who has granted bioRxiv a license to display the preprint in perpetuity. It is made available under aCC-BY-NC-ND 4.0 International license.

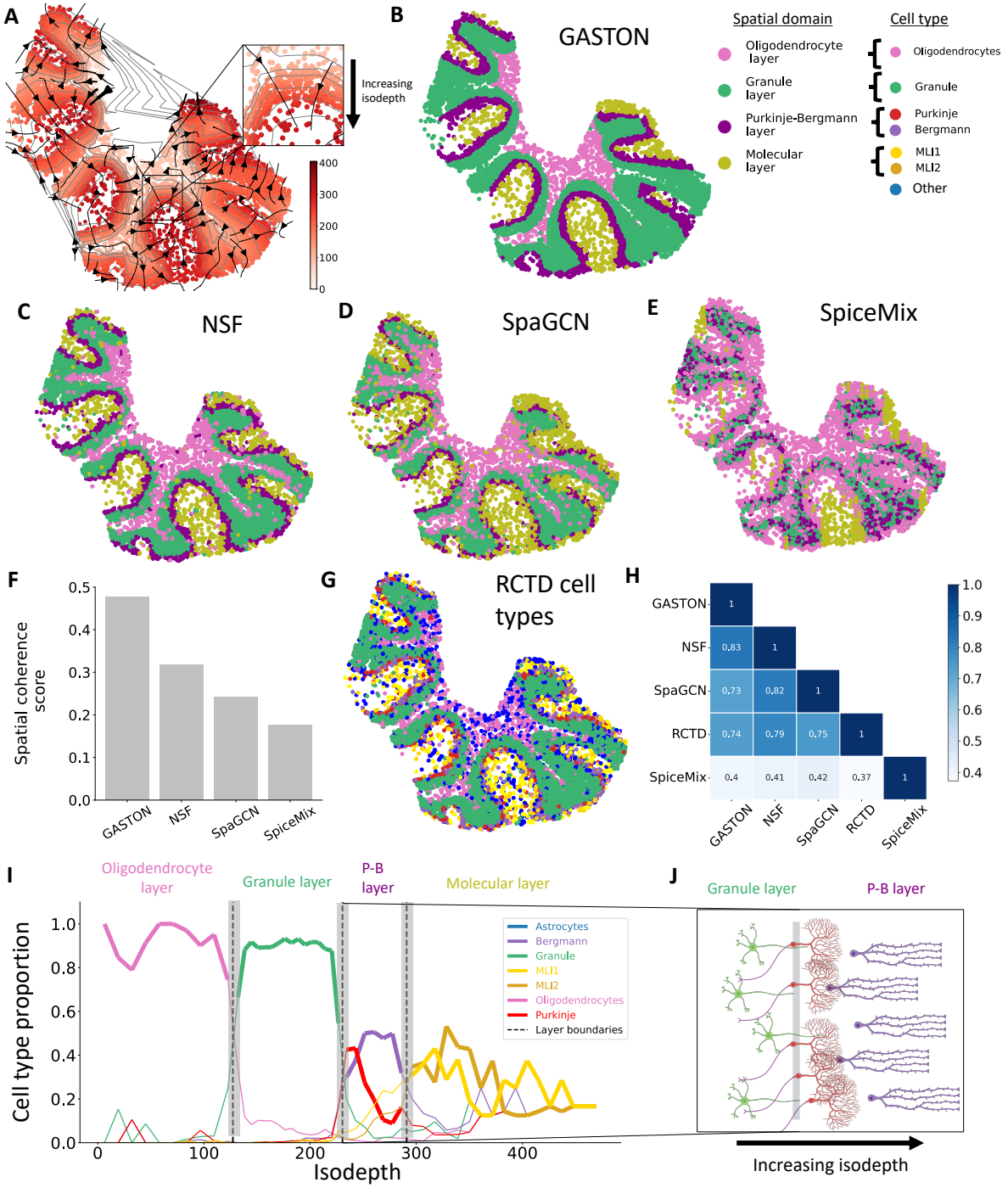

Figure 2: **Spatial gradients learned by GASTON recapitulate the spatial organization of the mouse cerebellum. (A)** The isodepth $d(x, y)$ and spatial expression gradients ∇d, shown as streamlines, learned by GASTON on Slide-SeqV2 data from the mouse cerebellum [18]. Gray curves denote contours of equal isodepth. **(B-E)** Spatial domains (layers) $R_1, \ldots, R_4$ identified using **(B)** GASTON, **(C)** Non-negative Spatial Factorization (NSF), **(D)** SpaGCN, and **(E)** SpiceMix. The spatial domains are colored according to the most prevalent RCTD cell types in the domain. **(F)** Spatial coherence score of spatial domains identified by each method. **(G)** Layer-specific cell types identified by RCTD. **(H)** F-measure between spatial domains identified by GASTON, NSF, SpaGCN, SpiceMix, and layer-specific cell types identified by RCTD. **(I)** Proportions of layer-specific cell types as a function of the isodepth d. Dashed lines indicate boundaries of GASTON spatial domains. **(J)** Layout of granule (green), Purkinje (red), and Bergmann (purple) cells as a function of isodepth near the Purkinje-Bergmann layer of the cerebellum.

bioRxiv preprint doi: https://doi.org/10.1101/2023.10.10.561757; this version posted October 13, 2023. The copyright holder for this preprint (which was not certified by peer review) is the author/funder, who has granted bioRxiv a license to display the preprint in perpetuity. It is made available under aCC-BY-NC-ND 4.0 International license.

edge [83, 84], which is difficult to obtain for a complex tissue like the cerebellum, or use scRNA-seq-based trajectory inference approaches which do not learn a spatially continuous measurement (see comparison to SpaceFlow [113] in Supplement C, Figure S1).

As additional validation, we evaluated GASTON using SRT data of the human dorsolateral prefrontal cortex (DLPFC) [89]. GASTON more accurately identified the manually annotated layers of the DLPFC compared to two graph neural network approaches: SpaGCN [58] and STAGATE [32] (Figure S3). Moreover, GASTON has comparable performance to Belayer [83], which previously achieved state-of-the-art performance in DLPFC layer identification using prior annotation on the layer boundaries. In contrast, GASTON, an unsupervised algorithm, achieves similar performance without any no prior knowledge. See Supplement D for details.

These analyses demonstrate that the isodepth d learned by GASTON provides a powerful computational approach for modeling the spatial organization of cells and cell types in complex biological tissues.

2.3 Continuous and discontinuous spatial variation in gene expression

We next investigated whether GASTON identifies biologically meaningful spatial patterns of gene expression in sparse SRT data, particularly in low coverage Slide-SeqV2 data (median $\approx$ 500 UMIs per spatial location [127]) where such patterns may not be apparent. For each gene g, GASTON learns a piecewise linear function $h_g(d)$ of the isodepth d that models both continuous variation in expression within or across spatial domains and sharp discontinuities in gene expression between adjacent spatial domains. These learned gene expression functions (Supplementary Table) indicate genes that have spatially varying expression patterns. For example, *SBK1* – reported to be a marker gene of Purkinje cells [71] – has particularly sparse expression in the Slide-SeqV2 cerebellum tissue, with only 15% of all spatial locations having non-zero UMI count, and only 2% of spatial locations in the GASTON-estimated Purkinje-Bergmann layer having UMI count > 1. (Figure 3A). By aggregating expression across contours of constant isodepth (Figure 2A), GASTON learns a piecewise linear gene expression function for *SBK1* that peaks in the Purkinje-Bergmann layer and exhibits continuous variation in the granule layer as a function of isodepth (Figure 3B). The corresponding 2D expression function clearly demarcates the Purkinje-Bergmann layer (Figure 3C) compared to the sparse expression values (Figure 3A).

The gene expression functions learned by GASTON yield a substantially better predictor of known marker genes in the cerebellum than existing methods for identifying spatially variable genes (SVGs) or differentially expressed genes (DEGs). Specifically, by ranking genes according to a measure of the variance of the GASTON expression function across spatial domains (Methods), GASTON achieved notably higher performance (AUPRC $\approx$ 0.31) in the identification of marker genes compared to HotSpot [31]; trendsceek [35]; SpatialDE [132]; SPARK-X [130, 171]; C-SIDE [18]; and SpaGCN [58] which have AUPRC ranging from 0.07 to 0.25 (Figure 3D). A major reason for GASTON's improved performance is because many of the other methods test only whether the expression of each gene varies in 2D space, and are unable to distinguish between different types of continuous and discontinuous variation in spatial expression. In contrast, GASTON's piecewise linear gene expression function explicitly models both continuous and discontinuous variation in expression. We highlight two genes ranked highly by GASTON but not by other methods: *SBK1*, described previously, and *FRMPD4*. *FRMPD4* is not a known marker gene but has high expression in the molecular layer (Figure 3E). Recent studies report that the *FRMPD4* protein regulates neurons in the molecular layer, with mutations of *FRMPD4* causing intellectual disabilities [105].

As another demonstration of the utility of the isodepth d learned by GASTON, we used the isodepth as a covariate for C-SIDE [18], which identifies cell type-specific differentially expressed (DE) genes from SRT data. This variation of C-SIDE, which we call C-SIDE-iso, identifies a substantially different set of DE genes compared to the original C-SIDE, with only a 10% overlap between the DE genes identified by both approaches. C-SIDE-iso achieved better performance than the original C-SIDE in marker gene

bioRxiv preprint doi: https://doi.org/10.1101/2023.10.10.561757; this version posted October 13, 2023. The copyright holder for this preprint (which was not certified by peer review) is the author/funder, who has granted bioRxiv a license to display the preprint in perpetuity. It is made available under aCC-BY-NC-ND 4.0 International license.

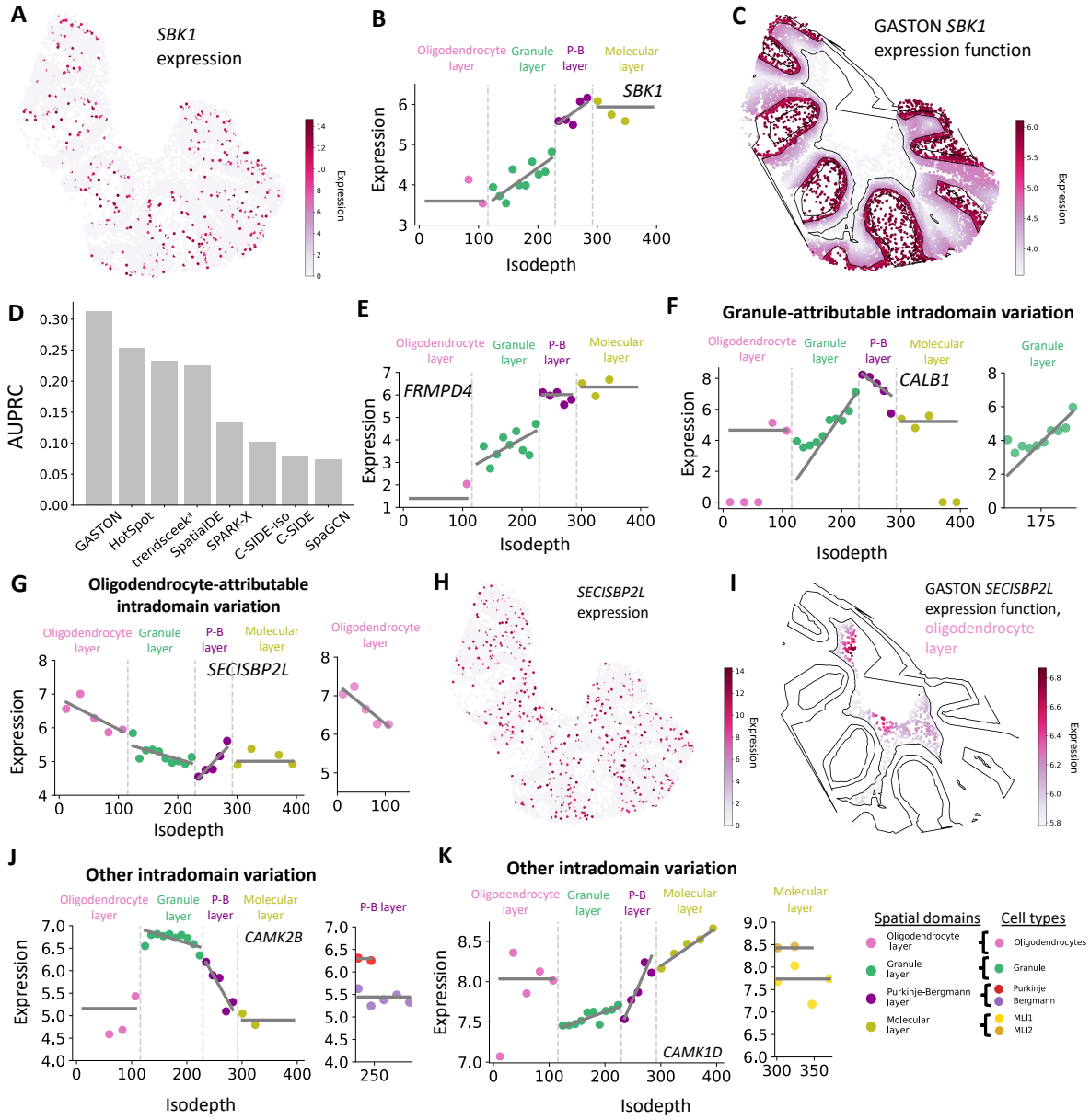

Figure 3: **GASTON reveals continuous and discontinuous spatial variation in gene expression in the mouse cerebellum. (A)** *SBK1* expression, shown in log counts per million (CPM). **(B)** Isodepth versus expression for *SBK1*. Lines denote piecewise linear function $h_g(d)$ learned by GASTON. **(C)** *SBK1* expression function $f(x, y)$ learned by GASTON. Curves denote contours of constant isodepth d. **(D)** Comparison of GASTON and several existing methods in marker gene identification, quantified using the area under precision-recall curve (AUPRC) and a list of known cerebellum marker genes [40, 71, 118, 69]. trendsceek* uses the Seurat [50] implementation and C-SIDE-iso runs C-SIDE using the isodepth d learned by GASTON as a covariate. **(E)** Isodepth versus expression for *FRMPD4* which was ranked highly by GASTON as a marker gene in (D). **(F)** (Left) Isodepth versus expression for *CALB1*, which has (Right) granule-attributable intradomain variation since the expression function restricted to granule cells has large slope. **(G)** (Left) Isodepth versus expression for *SECISBP2L* which has (Right) oligodendrocyte-attributable intradomain variation since the expression function restricted to oligodendrocyte cells has large slope. **(H)** *SECISBP2L* expression shown in log CPM. **(I)** *SECISBP2L* expression function $f(x, y)$ learned by GASTON in the GASTON-inferred oligodendrocyte layer. **(J-K)** Isodepth versus expression for **(J)** *CAMK2B* and **(K)** *CAMK1D* which have (Left) intradomain variation in the Purkinje-Bergmann layer and molecular layer, respectively, that is (Right) not attributable to cell type, as the expression functions for the most abundant cell types in the respective layers have zero slope.

bioRxiv preprint doi: https://doi.org/10.1101/2023.10.10.561757; this version posted October 13, 2023. The copyright holder for this preprint (which was not certified by peer review) is the author/funder, who has granted bioRxiv a license to display the preprint in perpetuity. It is made available under aCC-BY-NC-ND 4.0 International license.

identification (Figure 3C), demonstrating the advantages of the isodepth d. Nevertheless, unlike GASTON, C-SIDE-iso cannot identify spatial domains and thus cannot test for changes in expression across different spatial domains, and consequently C-SIDE-iso has lower performance than GASTON in identification of marker genes (Figure 3C).

In addition to marker gene identification, the piecewise linear expression functions learned by GASTON reveal distinct spatial patterns of gene expression including discontinuities in expression — i.e. large differences in expression between adjacent spatial domains — or continuous *intradomain* variation — i.e. a large slope β of the piecewise linear expression function within a spatial domain (Methods). GASTON identifies 513 spatially varying genes with either discontinuities or intradomain variation (Figure S2A). Approximately half of these genes have discontinuities in expression, indicating that a gene is selectively expressed or not expressed within cells in a specific spatial domain. For example, GASTON finds that *CPLX2* has discontinuities in expression at the boundaries of the granule layer, which matches prior studies showing that large expression of *CPLX2* in granule cells suppresses differentiation pathways [155] (Figure S2B). Furthermore, more than 60% of the spatially varying genes identified by GASTON have continuous intradomain variation (Figure S2A), indicating that continuous variation is fairly common in the cerebellum. This observation may explain why SpaGCN, whose clustering algorithm assumes there is no continuous variation in gene expression, is less accurate in resolving the layers of cerebellum layers (Figure 2D).

Continuous intradomain variation in gene expression may be due to a continuum of cell states within a cell type, continuous variation in the proportion of cell types in a tissue, or other causes [160]. We evaluated whether the intradomain variation identified by GASTON was attributable to the annotated cell types in each domain, which distinguishes whether there is (1) a spatial component in the continuum of cell states within a cell type [160] or (2) spatial variation in either the proportion of cell types or other causes (Methods). Specifically, we say that intradomain variation is *cell type-attributable* if the slope β_c estimated only from cells annotated as cell type c has magnitude $|\beta_c|$ close to or larger than the magnitude $|\beta|$ of the slope β estimated from all cells (Methods). We find that 217 of the 338 genes that GASTON reports to have intradomain variation have cell type-attributable intradomain variation (Figure S2A).

The cell type-attributable intradomain variation identified by GASTON reveals important cell type-specific processes including neuronal firing and differentiation. For example, *CALB1*, which is involved in calcium binding, has granule-attributable intradomain variation in the granule layer (Figure 3F). This granule-attributable *CALB1* continuous variation identified by GASTON provides a potential molecular explanation for the reported spatial gradients in neuronal firing thresholds for granule cells in the granular layer [128]. A second example is *SECISBP2L*, which exhibits large oligodendrocyte-attributable intradomain variation in the oligodendrocyte layer (Figure 3G). *SECISBP2L* was recently shown to be specifically expressed in differentiating oligodendrocytes, with *SECISBP2L* more highly expressed in less mature oligodendrocyte cells [29]. The observed decrease in *SECISBP2L* expression as a function of isodepth suggests that oligodendrocyte differentiation may occur along the isodepth axis, i.e. along the spatial gradients ∇d, in the oligodendrocyte layer (Figure 2A). Notably, continuous variation in *SECISBP2L* expression in the oligodendrocyte layer is not apparent from individual expression values per spot (Figure 3H), but is revealed by the expression function learned by GASTON, which pools expression values along contours of constant isodepth (Figure 3I).

Approximately 35% of the intradomain variation in gene expression identified by GASTON is not attributable to cell type (Figure S2A). For example, *CAMK2B*, which is overexpressed in granule cells, has large intradomain variation in the Purkinje-Bergmann layer (Figure 3J, left). However, this intradomain variation is not attributable to the Purkinje or Bergmann cell types, as the Purkinje- and Bergmann-specific expression functions for *CAMK2B* have zero slope (Figure 3J, right). Instead, the intradomain variation of *CAMK2B* is likely attributable to the large decrease in *proportion* of granule cells in the Purkinje-Bergmann layer as a function of isodepth (Figure 2I). *CAMK1D*, a calcium-dependent protein kinase whose aberrant

bioRxiv preprint doi: https://doi.org/10.1101/2023.10.10.561757; this version posted October 13, 2023. The copyright holder for this preprint (which was not certified by peer review) is the author/funder, who has granted bioRxiv a license to display the preprint in perpetuity. It is made available under aCC-BY-NC-ND 4.0 International license.

behavior has been linked to Alzheimer's disease [47] and glioma [63], exhibits intradomain variation in the molecular layer (Figure 3I, left) that is not attributable to either MLI1 or MLI2 neurons (Figure 3I, right). This variation could be attributable to other causes such as cellular interactions or neuronal firing.

These analyses demonstrate that GASTON's combined model of continuous and discontinuous variation of gene expression reveals biologically meaningful marker genes and continuous gradients of expression not found by existing approaches.

2.4 Spatial gradients in the tumor microenvironment

We next used GASTON to investigate spatial gene expression patterns in the tumor microenvironment (TME). The TME is strongly correlated with tumor development and prognosis [43], but is challenging to quantify accurately without spatial information [157]. However, existing analyses of tumor SRT data, e.g. [12, 36, 62], examine only differentially expressed (DE) genes or pathways between the tumor and surrounding stromal regions. We hypothesized that GASTON's ability to quantify continuous variation might reveal more subtle variation in gene expression relative to the boundary of the tumor.

We applied GASTON to SRT data from a colorectal (CRC) tumor tissue slice (Figure 4A) where the expression of 36,601 transcripts in 3,900 spots was measured using the 10x Genomics Visium platform [149]. GASTON identifies five spatial domains (Figure 4B) that are visually distinct in the H&E-stained image (Figure 4A), including the tumor (domain 1), the tumor-adjacent stromal region (domain 2), and other stromal regions not directly adjacent to the tumor (domains 3-5). In contrast, the the published analysis of this data performed unsupervised clustering of spots based on gene expression alone [121] and was unable to distinguish between the different stromal regions of the the tissue slice (Figure S4).

We analyzed spatial variation in the TME by examining the expression of each gene as a function of the isodepth d, which varies smoothly from the tumor boundary to the interior (Figure 4C, Supplementary Table). GASTON identifies 1,572 spatially varying genes in the tumor and adjacent stromal domains which exhibit one of seven different spatial expression patterns: intratumoral variation, a discontinuity at the tumor-stroma boundary, intrastromal variation, or any combination of these (Figure 4D). For six of the seven spatial gene expression patterns, the genes exhibiting the spatial pattern are enriched ($p < 0.01$, GSEA [74]) for cancer hallmark gene sets (Figure 4E). We further group the genes in the six enriched spatial gene expression patterns found by GASTON into three different types: (1) Type I genes, which have intratumoral variation and no discontinuity in expression; (2) Type II genes, which have intrastromal variation and a discontinuity at the tumor-stroma boundary; and (3) Type III genes, which have either intrastromal variation or discontinuity at the tumor-stroma boundary but no intratumoral variation.

The three types of spatially varying genes identified by GASTON reflect distinct biological processes occurring in the TME. The 742 Type I genes (intratumoral variation) are enriched for oxidative phosphorylation and cholesterol homeostasis gene sets; moreover, 39 of the 42 Type I genes involved in oxidative phosphorylation or cholesterol homeostasis have *positive* slopes within the tumor domain, indicating an increase in expression from the margin to the interior of the tumor. Thus, Type I genes likely indicate an *increasing* gradient of metabolic activity from the tumor boundary to the interior [74]. For example, *COX7B* (Figure 4F) is a Type I gene in the oxidative phosphorylation pathway and a component of the cytochrome c oxidase protein complex which transfers electrons to oxygen in the electron transport chain and leads to ATP synthesis [144]. Several other genes in this complex are also Type I genes, including *COX17*, *COX7A2*, *COX6C*, and *COX8A*. Another Type I gene is Stearyl-CoA desaturase (*SCD*, Figure 4G), a fatty enzyme that is key component of lipid metabolism [122], with *SCD* deficiency being linked to reduced lipid synthesis and other poor health outcomes [38]. Interestingly, the expression of both *SCD* and *COX7B* are directly affected by oxygen availability [151], with lower expression in hypoxic conditions. The higher expression of these genes in the interior of the tumor suggests that the interior of this CRC tumor slice is more oxygenated than the boundary. This observation is consistent with a previous clinical study

bioRxiv preprint doi: https://doi.org/10.1101/2023.10.10.561757; this version posted October 13, 2023. The copyright holder for this preprint (which was not certified by peer review) is the author/funder, who has granted bioRxiv a license to display the preprint in perpetuity. It is made available under aCC-BY-NC-ND 4.0 International license.

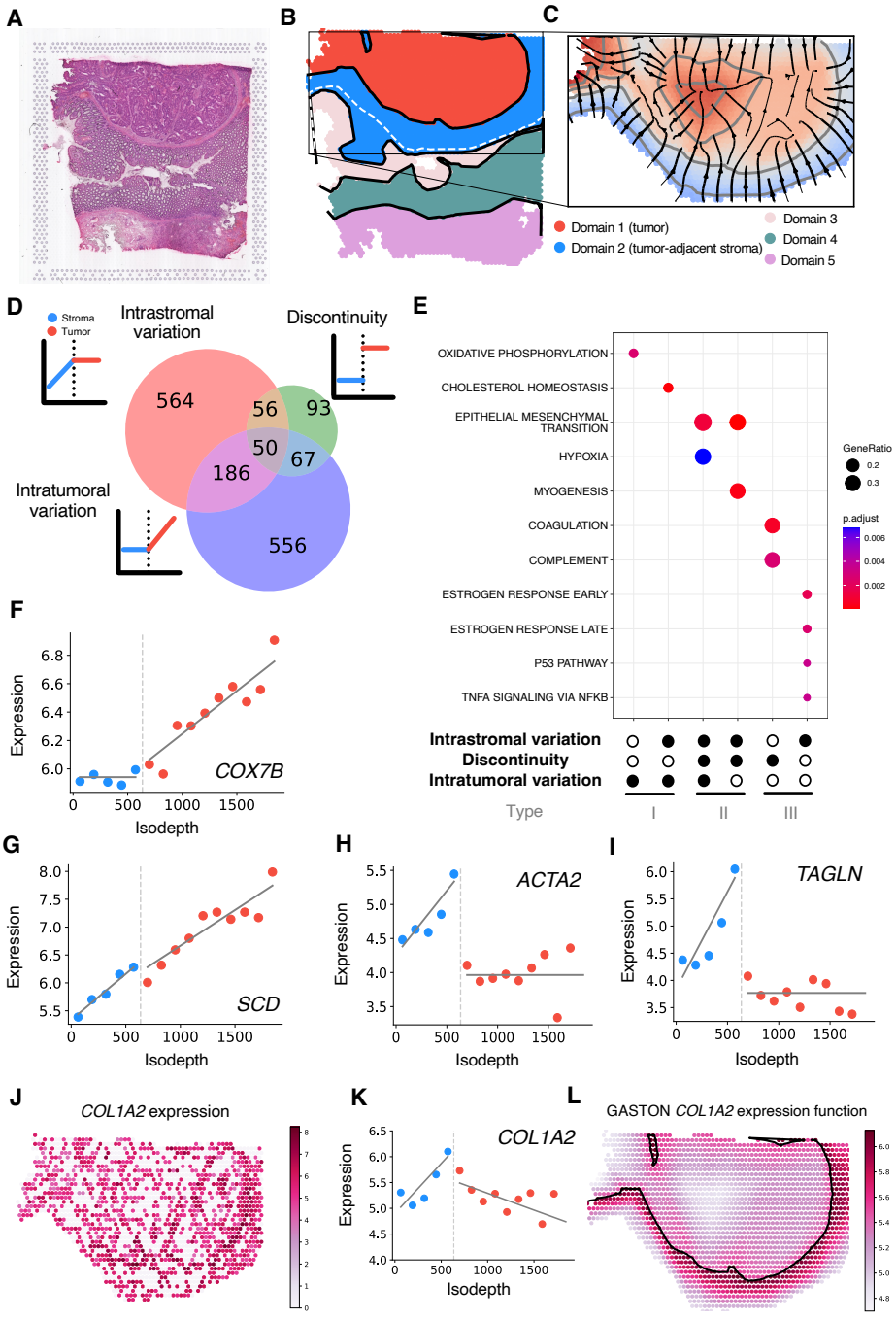

Figure 4: **GASTON identifies spatial gene expression patterns in the tumor micro-environment.** **(A)** H&E stain of a 10x Genomics Visium colorectal tumor sample. **(B)** Spatial domains learned by GASTON. Domains 1 and 2 are labeled as tumor and tumor-adjacent stroma, respectively, based on the histology image in (A). **(C)** Isodepth d and spatial gradients learned by GASTON restricted to tumor and tumor-adjacent stromal domains. **(D)** GASTON identifies 986 spatially varying genes which are classified into three spatial expression patterns: genes with intrastromal variation in expression; genes with a discontinuity in expression at the tumor-stroma boundary; and genes with intratumoral variation in expression. **(E)** Enrichment for hallmark cancer gene sets reported by gene set enrichment analysis (GSEA) for six of the seven spatial expression patterns in (D). The spatial expression patterns are grouped into three types according to expression pattern and enriched cancer pathways. **(F-I)** Isodepth d versus expression for Type I genes **(F)** *COX4l1* and **(G)** *SCD*, and Type II genes **(H)** *ACTA2* and **(I)** *TAGLN*. **(J)** *COL1A2* expression shown in log CPM. **(K)** Expression versus isodepth for Type II gene *COL1A2*. **(L)** GASTON *COL1A2* expression function shows a gradient of expression at the tumor-stroma boundary.

bioRxiv preprint doi: https://doi.org/10.1101/2023.10.10.561757; this version posted October 13, 2023. The copyright holder for this preprint (which was not certified by peer review) is the author/funder, who has granted bioRxiv a license to display the preprint in perpetuity. It is made available under aCC-BY-NC-ND 4.0 International license.

which found that that stage IV CRC tumors may have lower hypoxia response — and thus higher oxygen availability — in the tumor interior compared to the boundary [2].

The 106 Type II genes (intrastromal variation and discontinuity) primarily describe the upregulation of epithelial-mesenchymal transition (EMT) genes immediately outside the tumor boundary. Several studies have shown that upregulation of EMT genes within tumor-associated stromal cells is associated with aggressive, poor prognosis CRC subtypes [20, 60, 73]. Of the 15 type II genes in the EMT pathway, 14 had positive slopes with isodepth in the tumor-adjacent stroma domain, i.e. expression increased closer to the tumor boundary, suggesting that this stage IV colorectal tumor was likely an aggressive subtype. For example, *ACTA2* and *TAGLN*, two genes that were reported to be markers of a subtype of colorectal cancer-associated fibroblasts with upregulated EMT-related genes [73], have positive slopes and large discontinuities at the tumor boundary (Figure 4H, I). GASTON also finds that *ACTA2* and *TAGLN* have constant, low expression in the tumor region, consistent with previous studies that find no evidence for upregulation of EMT-related genes in CRC tumor cells [20, 60]. The upregulation of EMT genes – such as *ACTA2* and *TAGLN* – in tumor-associated stromal cells could be an important mechanism underlying the aggressiveness of this CRC tumor, where these stromal cells may facilitate local invasion and metastasis [65]. Notably, the overexpression of several Type II genes is concentrated on the right side of the tumor boundary (Figure S5A,B), suggesting that the local invasion and metastasis may be localized to a specific part of the tumor boundary. We also highlight the Type II gene *LGR5*, which has large expression at the tumor boundary and has been reported to be a potential marker for CRC stem cells [92] (Figure S5C,D). The co-expression of *LGR5* and *ACTA2* / *TAGLN* suggests a potential interaction between tumor-adjacent stromal cells and CRC stem cells.

We emphasize that the upregulation of EMT genes near the tumor boundary is not readily apparent from the sparse UMI counts. For example, *COL1A2* is a Type II gene involved in EMT [146], but the spatial distribution of *COL1A2* expression is difficult to discern directly (Figure 4J), with nearly half of all spots having no measured *COL1A2* transcripts while only a small fraction of spots (5%) have more than 10 transcripts. GASTON aggregates the sparse *COL1A2* expression measurements across the contours of constant isodepth and learns a piecewise linear *COL1A2* expression function of isodepth (Figure 4K), revealing continuous variation in *COL1A2* expression. In particular, GASTON finds that *COL1A2* expression peaks at the tumor boundary and decays in the interior of tumor and in the tumor-adjacent stroma (Figure 4L). This expression pattern is consistent with a recent report demonstrating that *COL1A2* expression is lower in primary CRC tumors compared to adjacent stromal tissue [156].

The 657 Type III genes (no intratumoral variation) identified by GASTON primarily describe immune response in the stroma as well as cell signaling and proliferation in the tumor. For example, *THBS1* has a large discontinuity in expression at the tumor-stroma boundary and has high expression in the tumor-adjacent stroma (Figure S5E), consistent with reports that *THBS1* expression promotes immune cell response in other cancer types [106, 166]. Another Type III gene, *FUCA1*, is involved in fucosylation of proteins and a member of the p53 signaling pathway [37]. GASTON finds that *FUCA1* has large, negative slope in the stroma region; no discontinuity in expression at the tumor boundary; and constant, low expression in the tumor region (Figure S5F). This spatial expression pattern suggests that *FUCA1* is downregulated in the tumor region, agreeing with several recent studies which found that *FUCA1* is downregulated in highly aggressive and metastatic CRC and breast tumors [16, 99].

Overall, the spatial gene expression patterns identified by GASTON suggest that the interior of this CRC tumor sample is growing slowly – since aerobic metabolism through oxidative phosphorylation indicates slow cellular growth and proliferation [169] – while the boundary is undergoing EMT to stem-like states [86]. These features of the tumor interior and boundary indicate a late-stage, vascularized primary tumor with a fully metastatic margin, a characterization which aligns with the tumor's clinical information [149]. Thus, this analysis demonstrates how the gene expression topography learned by GASTON enables the characterization of the spatial and molecular organization of the TME.

bioRxiv preprint doi: https://doi.org/10.1101/2023.10.10.561757; this version posted October 13, 2023. The copyright holder for this preprint (which was not certified by peer review) is the author/funder, who has granted bioRxiv a license to display the preprint in perpetuity. It is made available under aCC-BY-NC-ND 4.0 International license.

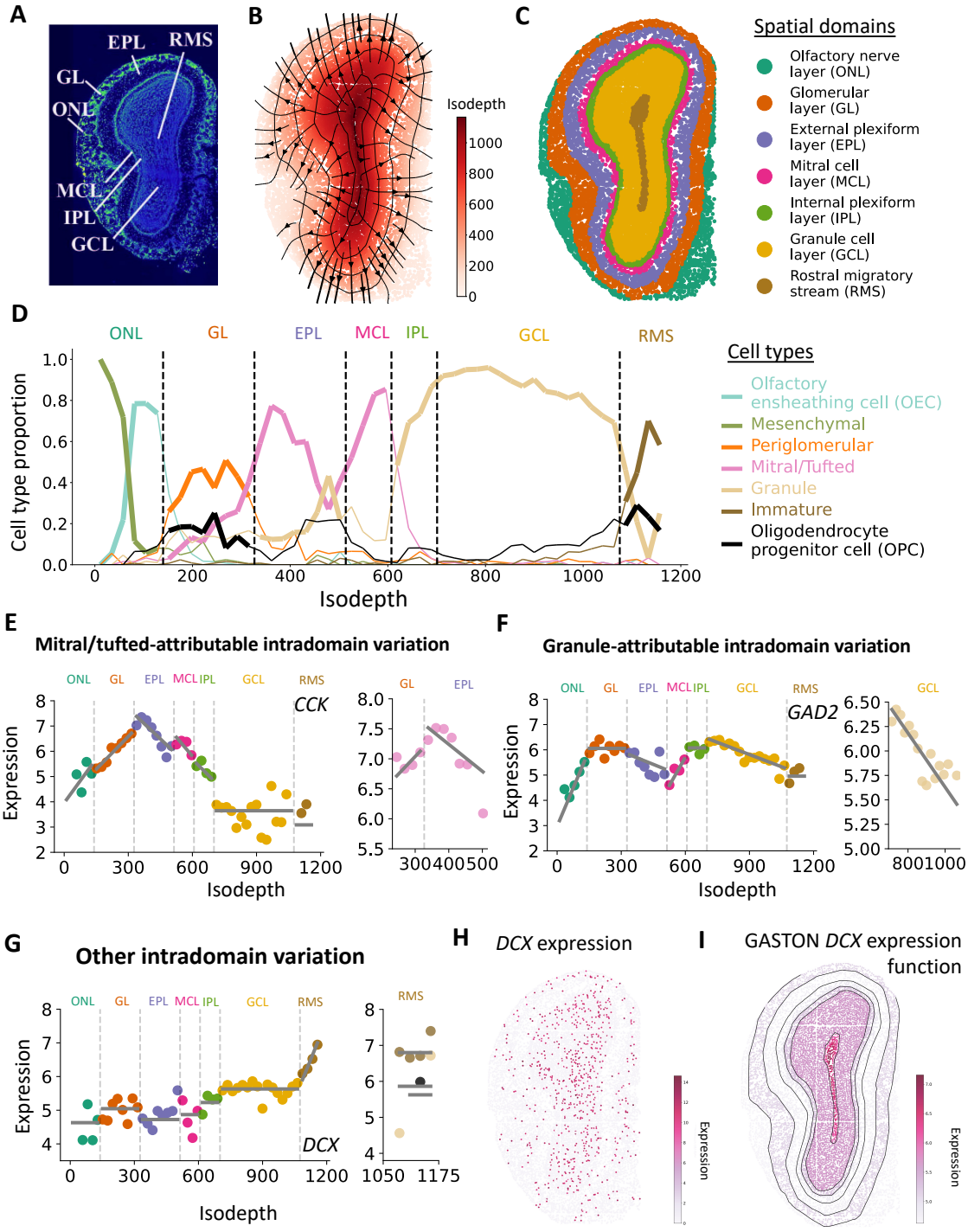

Figure 5: **GASTON reveals variation in cell types and gene expression in the mouse olfactory bulb.** **(A)** DAPI stain of mouse olfactory bulb [42] produced by [22]. **(B)** Isodepth d and (negative) spatial gradients $-\nabla d$ (shown as streamlines) learned by GASTON. Curves denote contours of constant isodepth d. **(C)** Spatial domains learned by GASTON and labeled based on annotations in (A). **(D)** Cell type proportion as a function of isodepth d. Dashed lines indicate boundaries of spatial domains identified by GASTON. Most abundant cell types in each spatial domain are highlighted. **(E)** (Left) Isodepth versus expression for *CCK* which (Right) has mitral/tufted-attributable intradomain variation in the glomerular layer (GL) and external plexiform layer (EPL). **(F)** (Left) Isodepth versus expression for *GAD2* which (Right) has granule-attributable intradomain variation in the granule cell layer (GCL). **(G)** (Left) Isodepth versus expression for *DCX* which has continuous variation in the rostral migratory stream (RMS) which is (Right) not attributable to cell type, as the expression function for the most abundant cell types have zero slope. **(H)** *DCX* expression shown in log CPM. **(I)** *DCX* expression function learned by GASTON.

bioRxiv preprint doi: https://doi.org/10.1101/2023.10.10.561757; this version posted October 13, 2023. The copyright holder for this preprint (which was not certified by peer review) is the author/funder, who has granted bioRxiv a license to display the preprint in perpetuity. It is made available under aCC-BY-NC-ND 4.0 International license.

2.5 Spatial gradients of cell type and gene expression in the mouse olfactory bulb

Finally, we used GASTON to analyze Stereo-seq [22] data from the mouse olfactory bulb which measures the expression of 27,106 transcripts at 9,825 spatial locations. Stereo-seq achieves single cell spatial resolution using DNA nanoball patterned array chips, but the data is highly sparse, with a median UMI of less than 350 per location. At the same time, the olfactory bulb has a *radial* geometry consisting of several concentric layers (Figure 5A), and this geometry provides spatial constraints that may help overcome the severe data sparsity.

GASTON learns the radial geometry of the olfactory bulb nearly perfectly, with the isodepth d providing a topographic map that reflects the geometry of the olfactory bulb (Figure 5B). Using the learned isodepth, GASTON divides the tissue into seven contiguous spatial domains (Figure 5C) that visually correspond to the seven distinct layers of the olfactory bulb (Figure 5A). In comparison, the spatial domains found by SpaGCN, a method based on a graph convolutional neural network, are less spatially coherent than the GASTON domains and do not reflect the layered geometry of the olfactory bulb. Notably, SpaGCN poorly resolves the innermost rostral migratory stream (RMS) layer (Figure S6A,B).

The olfactory bulb is one of two regions in the brain where adult neurogenesis occurs, with immature neurons migrating outward from the RMS (large isodepth) towards the outermost olfactory nerve layer (ONL, small isodepth) [90, 80]. Thus, in this tissue, the isodepth d learned by GASTON provides a measure of *potency* in the olfactory bulb, and the negative gradients $-\nabla d$ show the spatial trajectories of neural maturation and migration (Figure 5B).

GASTON reveals substantial variation in cell type composition as a function of isodepth d in the olfactory bulb (Figure 5D). While the cell type composition of the different layers of the olfactory bulb is well-studied, GASTON uncovers the spatial arrangement of cell types within each layer which has not been fully characterized in the literature [94]. For example, while previous studies have found that both mesenchymal cells and olfactory ensheathing cells (OECs) are in the outermost olfactory nerve layer (ONL) [75], GASTON identifies that these two cell types have different spatial arrangements in the ONL: mesenchymal cells are concentrated on the outer edge of the layer (isodepth $d < 50$) while OECs peak at a larger isodepth ($d \approx 85$) and are spread more diffusely throughout the ONL. This arrangement of mesenchymal cells aligns with studies showing that ONL neuron axons grow towards mesenchymal cells during development [33, 109], as axons in the olfactory bulb point outwards [75], i.e. towards small isodepth. In the interior of the olfactory bulb, GASTON finds that immature neurons are most prevalent in the rostral migratory stream (RMS), with the proportion of immature neurons increasing sharply with isodepth, in agreement with studies showing that neurogenesis occurs starting from the RMS interior [90, 80].

The isodepth d also distinguishes different cell types or cell states with similar gene expression profiles. For example, mitral cells and tufted cells are grouped together in the single-cell reference dataset [133] used for cell type annotation, and also by SpaGCN (Figure S6A), due to the similar gene expression profiles of these cell types. However, GASTON reveals that the proportion of mitral/tufted cells peaks at two different isodepth values, $d \approx 350$ and $d \approx 600$, with a larger proportion of mitral/tufted cells at the second peak versus the first peak (Figure 5D). This suggests that the mitral/tufted cells at isodepth $d \approx 350$ are tufted cells, which previous studies have shown are spread diffusely in the external plexiform layer (EPL) [94], while the mitral/tufted cells at isodepth $d \approx 600$ are mitral cells, which have been shown to form a monolayer in the mitral cell layer (MCL) [41]. GASTON also distinguishes between different granule cell states. While there is a single category of granule cells in the single-cell reference dataset [133], previous studies have shown that there are morphologically distinct granule cell subtypes in different layers of the olfactory bulb [94]. GASTON shows that while granule cells are most prevalent in the granule cell layer (GCL), there is a small population of granule cells in the EPL and in the MCL with roughly constant cell type proportion (Figure 5D). The spatial segregration of these two granule cell populations suggests that the granule cells in the EPL and MCL may have a different cell state compared to granule cells in the GCL.

bioRxiv preprint doi: https://doi.org/10.1101/2023.10.10.561757; this version posted October 13, 2023. The copyright holder for this preprint (which was not certified by peer review) is the author/funder, who has granted bioRxiv a license to display the preprint in perpetuity. It is made available under aCC-BY-NC-ND 4.0 International license.

Notably, neither the distinction between mitral and tufted cells nor the prevalence of immature neurons in the interior of the bulb are apparent using an alternative 1-D coordinate computed by SpaceFlow [113] that is based on diffusion pseudotime [49] (Supplementary Section C and Figure S6).

GASTON identifies 704 genes with spatially varying expression – i.e. genes with either discontinuous expression or intradomain variation in expression – in the olfactory bulb (Figure S7, Supplementary Table). These genes distinguish different cell types and states in the olfactory bulb and reveal potential molecular mechanisms for biological phenomena. We highlight three examples here. *CCK*, which is reported to be a marker for a specific subtype of tufted cells [163, 131, 59], has mitral/tufted-attributable intradomain variation in the glomerular layer (GL) and EPL (Figure 5E). As noted above, the mitral/tufted cells in the GL and EPL are likely tufted cells, indicating that the continuous variation in *CCK* expression is likely tufted cell-attributable and not mitral cell-attributable. *GAD2*, a marker gene for neurons in the GABAergic systems – the main inhibitory neurotransmitter system in the brain [8, 14, 10] – has granule-attributable intradomain variation in the GCL (Figure 5F). Granule cells are known to be GABAergic [94], suggesting that the granule-attributable variation identified by GASTON may play a role in the GABAergic system. *DCX* (doublecortin) has large intradomain variation in the RMS (Figure 5G), consistent with reports [39, 45] that *DCX* is a marker gene for immature neurons in the RMS (Figure 5D). The continuous variation in *DCX* expression is not attributable to cell type, and instead is likely due to the increasing *proportion* of immature neurons in the RMS as a function of isodepth (Figure 5D). While the intradomain variation in *DCX* expression is challenging to observe from the sparse Stereo-seq UMI counts (Figure 5H), GASTON learns a *DCX* expression function that pools expression across isodepth and uncovers the continuous intradomain variation in *DCX* (Figure 5I).

3 Discussion

Accurate models of spatial gene expression variation within tissues are critical for determining the spatial organization of cell types and for defining processes of differentiation and intercellular communication that modulate cell states within spatial niches. Spatial variation in gene expression includes both discontinuous changes in gene expression across the different spatial domains of a tissue, as well as continuous variation within and across spatial domains due to variation in cell state or other causes. While numerous computational methods have been developed to identify spatial domains by modeling discontinuous changes in gene expression, few methods are able to identify spatial domains and *simultaneously* model continuous variation within the domains. Moreover, to our knowledge no existing methods perform this simultaneous identification in an unsupervised and biologically interpretable manner.

In this work, we introduce the *isodepth*, a coordinate that models both the arrangement of spatial domains within a tissue and the relative position of spatial locations with each domain. The isodepth gives a *topographic map* of a tissue slice, analogous to elevation in a map of the Earth's surface. The gradient of the isodepth describes *spatial gradients*, or the spatial directions of maximum change in gene expression in a tissue. We derive an unsupervised and interpretable deep learning algorithm, GASTON, that learns the isodepth, spatial gradients, and piecewise linear gene expression functions of the isodepth. We demonstrate that the isodepth and spatial gradients learned by GASTON improve detection of spatial domains and spatially varying marker genes, and enable the identification of spatial gene expression patterns linked to important biological processes including differentiation and communication in the brain as well as hypoxia in the tumor microenvironment.

A key advantage of the isodepth computed by GASTON is that it provides a *global* model of spatial gene expression. Just as one can climb to the same elevation on two different mountains, so too can the isodepth take on the same value at two spatially separated locations in the same spatial domain, e.g. the Purkinje-Bergmann layer in the mouse cerebellum (Figure 2B). This global model presents a stark departure from

bioRxiv preprint doi: https://doi.org/10.1101/2023.10.10.561757; this version posted October 13, 2023. The copyright holder for this preprint (which was not certified by peer review) is the author/funder, who has granted bioRxiv a license to display the preprint in perpetuity. It is made available under aCC-BY-NC-ND 4.0 International license.

nearly all existing SRT methods which model only *local* spatial correlations. Using the isodepth, GASTON is able to model *"long-range"* spatial correlations, i.e. correlations between distant spatial locations, and pool information across spatially distant locations on the same isodepth contour. As we demonstrate, incorporating these long-range dependencies leads to improved inference of spatial domains and marker genes.

On a smaller scale, the isodepth learned by GASTON provides a coordinate for quantifying variation in gene expression in the tumor microenvironment (TME). Just as single-cell transcriptomics of tumor samples led to the identification of numerous clinical and molecular biomarkers [158], we anticipate that spatial variation in gene expression in the TME will also have high clinical relevance. For example, we showed that GASTON extracts gradients in gene expression that correlate with metabolism, the epithelial-mesenchymal transition (EMT) and other hallmarks of the TME which may translate to novel biomarkers for prognostics, treatment outcome prediction, and personalized medicine [28, 57, 44]. Additionally, GASTON introduces a new axis of tumor classification, in which tumors may be further characterized by the variation of distinct tumor processes across spatial gradients; for example, some tumors may have an increasing gradient of aerobic metabolism towards the tumor center (e.g. Figure 4) while other tumors may have a decreasing gradient. Another potential clinical implication is that the spatial gradients learned by GASTON could reveal spatial trajectories of *metastatic* migration, similar to how the spatial gradients learned by GASTON in the olfactory bulb show spatial trajectories of neural migration (Figure 5B). For example, the variation of EMT genes along the spatial gradients near the tumor boundary may reveal the molecular underpinnings of the *margination* process in which tumor cells migrate towards a vascular wall before metastasis [142, 165].

The inference of continuous variation in *transcriptomic* space, i.e. trajectory inference or *pseudotime* approaches, is widely applied in scRNA-seq analysis [49, 137, 107, 129]. Recently, there have been some attempts to adapt these approaches to SRT data [113, 51, 97, 85]. However, continuous variation in transcriptomic space is not equivalent to continuous variation in *physical* space that is modeled by isodepth. Indeed we find that existing approaches based on diffusion pseudotime [49] learn a coordinate that is nearly constant in each spatial domain, and thus obscures spatial variation in gene expression and cell type proportions within spatial domains (Figure S6). This limitation of existing scRNA-seq-based approaches underscores the need for methods like GASTON that model continuous *spatial* variation.

We note that the current derivation of isodepth by GASTON relies on two simplifying assumptions that may require adjustment for specific applications. First, we assume that all (spatially varying) genes share the same vector field of spatial gradients. Thus, GASTON will not automatically find multiple directions of spatial variation, where each direction corresponds to a subset of genes. For these situations, it might be appropriate to learn the isodepth using a restricted set of genes or a smaller region of a tissue slice; e.g. one may apply GASTON to spatial domains or gene sets obtained from a standard SRT or single-cell clustering algorithm. Second, we assume that the shared spatial gradient vector field is *conservative*, meaning that it does not "rotate" in space (i.e. $\text{curl}(\mathbf{v}) = 0$). GASTON may not be applicable to tissue slices where this assumption is violated, although we are not aware of any such biological examples. An important next step would be to develop a framework for learning spatial gradients under relaxed mathematical assumptions, potentially using neural fields or transformers which have been used to learn vector fields in other areas of biology and machine learning [110, 152, 23].

We envision that the simplicity and generality of both the mathematical framework of the isodepth and the GASTON algorithm can be readily extended in several directions. First, the piecewise linear model of gene expression can be replaced by more complicated functions. While more complicated functions may be prone to overfitting with sparse SRT data, they may be appropriate for targeted SRT technologies — e.g. MERFISH [91], 10X Genomics Xenium [61], STARMap [143, 162], or NanoString CosMx [52] — that have higher detection efficiency. Second, it would be desirable to extend GASTON to identify 3-D spatial gradients, e.g. by utilizing spatial alignment tools [159, 77, 67, 64], as well as spatiotemporal gradients

bioRxiv preprint doi: https://doi.org/10.1101/2023.10.10.561757; this version posted October 13, 2023. The copyright holder for this preprint (which was not certified by peer review) is the author/funder, who has granted bioRxiv a license to display the preprint in perpetuity. It is made available under aCC-BY-NC-ND 4.0 International license.

[114]. A third direction is to extend GASTON to other molecular modalities such as chromatin accessibility [164, 119] or protein/metabolite abundance [141, 82], e.g. using recent data on spatial measurements of ribosome-bound transcripts [161]. Fourth, there has been much work on quantifying transcriptomic vector fields by computing RNA velocity from ratios of spliced/unspliced RNA in single-cell RNA-seq data (e.g. [108, 70, 46, 11]) and it would be interesting to understand how RNA velocity varies along the spatial gradients learned by GASTON. Similarly, it would also be useful to understand how local microenvironments or cellular interactions, e.g. as learned by [150, 112, 30], vary along the GASTON spatial gradients. Finally, several recent papers have studied how genetic variants affect single-cell gene expression measurements, i.e. single-cell eQTLs (expression quantitative trait loci) [27, 95] and it would be useful to understand how genetic variants contribute to the continuous and discontinuous spatial gene expression patterns found by GASTON.

In summary, the topographic maps and gene expression functions computed by GASTON provide a novel and general framework for analyzing continuous and discontinuous spatial variation in gene expression from spatial sequencing data across many biological systems.

bioRxiv preprint doi: https://doi.org/10.1101/2023.10.10.561757; this version posted October 13, 2023. The copyright holder for this preprint (which was not certified by peer review) is the author/funder, who has granted bioRxiv a license to display the preprint in perpetuity. It is made available under aCC-BY-NC-ND 4.0 International license.

4 Methods

4.1 Modeling gene expression and spatial gradients

We derive a model for spatial domains and gradients of gene expression in spatially resolved transcriptomics (SRT) data. SRT technologies measure the expression of G genes in a tissue slice $T \subseteq \mathbb{R}^2$, which we model with a *gene expression function* $\mathbf{f} : T \to \mathbb{R}^G$. The vector $\mathbf{f}(x, y) = (f_1(x, y), \ldots, f_G(x, y))^\intercal$ gives the (normalized) expression of each gene at spatial location (x, y) in the tissue slice T, with the g-th component function $f_g : \mathbb{R}^2 \to \mathbb{R}$ describing the expression of a single gene g. For example, a gene g whose expression is constant across the tissue slice T has a constant expression function $f_g(x, y) = c$, while a gene that is differentially expressed in a region $R \subseteq T$ might have the expression function $f_g(x, y) = c \cdot 1_{\{(x,y)\in R\}} + c' \cdot 1_{\{(x,y)\notin R\}}$.

We model each expression function f_g as a *piecewise continuous* function. Piecewise continuous functions model continuous spatial variation in gene expression while also allowing for discontinuities in expression due to sharp changes in cell type composition or other factors. We assume the expression functions f_g have the same pieces for all genes, and thus each expression function f_g has the form:

$$f_g(x, y) = \sum_{p=1}^{P} f_{g,p}(x, y) \cdot 1_{\{(x,y)\in R_p\}}. \tag{2}$$

where $f_{g,p} : \mathbb{R}^2 \to \mathbb{R}$ are continuous functions and $R_1, \ldots, R_P \subseteq \mathbb{R}^2$ are a partition of the tissue slice T into P disjoint regions which we call *spatial domains*. Note that the spatial domains R_p need not be contiguous, and thus this model allows for physically separate locations within the tissue slice to contain a similar composition of cell types.

A *spatial gradient* describes how gene expression varies across the 2D tissue slice T. For a single gene g, the spatial gradient is given by the gradient ∇f_g of the expression function f_g. More generally, the rows of the Jacobian matrix $\mathbf{J}(\mathbf{f}) = \left[\nabla f_1 \ \cdots \ \nabla f_G\right]^\intercal \in \mathbb{R}^{G\times 2}$ of the gene expression function $\mathbf{f}$ give the individual spatial gradient of each gene at each spatial location $(x, y) \in T$. Note that the rank of the Jacobian matrix $\mathbf{J}(\mathbf{f})$ is at most two.

Estimating the spatial gradients ∇f_g for every gene g from SRT data from a single tissue slice is difficult due to the limited spatial resolution and limited sequence coverage (e.g. sparsity) of the data. To avoid overfitting, we make some assumptions on the structure of the spatial gradients. Specifically, we assume that the Jacobian matrix $\mathbf{J}(\mathbf{f})$ has *rank one* at every spatial location $(x, y) \in T$, i.e. the rows $\nabla f_g(x, y)$ of the Jacobian matrix $\mathbf{J}(\mathbf{f})(x, y)$ are linearly dependent for every spatial location $(x, y) \in T$. This assumption is motivated by the observation that spatial expression gradients tend to be correlated; for example, many genes have been observed to have expression gradients along the same axes in the brain and liver [21, 9]. Under this assumption, for each spatial location $(x, y) \in T$ there exists a vector $\mathbf{v}(x, y) \in \mathbb{R}^2$ such that the gradient vector $\nabla f_g(x, y)$ of each gene g is a scalar multiple of the vector $\mathbf{v}(x, y)$:

$$\nabla f_g(x, y) = \beta_g(x, y) \cdot \mathbf{v}(x, y) \tag{3}$$

where $\beta_g(x, y) : \mathbb{R}^2 \to \mathbb{R}$ are scalar functions and $\mathbf{v}(x, y)$ is a vector field which we call the *spatial gradient vector field*. Since the expression function $\mathbf{f}$ is piecewise continuous, the gradient ∇f_g of each expression function f_g is also piecewise continuous, and so we may re-write (3) as

$$\nabla f_g(x, y) = \sum_{p=1}^{P} \beta_g(x, y) \cdot \mathbf{v}(x, y) \cdot 1_{\{(x,y)\in R_p\}}. \tag{4}$$

bioRxiv preprint doi: https://doi.org/10.1101/2023.10.10.561757; this version posted October 13, 2023. The copyright holder for this preprint (which was not certified by peer review) is the author/funder, who has granted bioRxiv a license to display the preprint in perpetuity. It is made available under aCC-BY-NC-ND 4.0 International license.

4.2 Conservative vector fields and piecewise linear functions

Equation (4) provides a general model for spatial gradients ∇f_g under a rank-one assumption on the Jacobian matrix $\mathbf{J}(\mathbf{f})$. However, in practice, it is still difficult to estimate the parameters of (4) from SRT data, as we do not observe expression gradients ∇f_g but only the expression values f_g. To derive a model for the expression functions f_g while minimizing overfitting, we make three simplifying assumptions on the spatial gradient vector field $\mathbf{v}$, spatial domains R_p, and scalar functions $\beta_g(x, y)$.

First, we assume the spatial gradient vector field $\mathbf{v}$ is the gradient of a continuously differentiable, scalar function $d : \mathbb{R}^2 \to \mathbb{R}$, i.e. $\mathbf{v} = \nabla d$. We call d the *isodepth* of the tissue slice T. The isodepth d describes the "topography" of a tissue slice T, analogous to the elevation in a topographic maps of a geographic region. In physics, vector fields $\mathbf{v}$ that are the gradient of a scalar function d are called *conservative* vector fields, and the scalar function d is called the potential function as it measures potential energy at different locations in space, e.g. a gravitational potential function or an electric potential function [87]. In our setting, the scalar function d measures a *"gene expression potential"* at different locations in a tissue slice T. The vector field $\mathbf{v}$ being conservative is equivalent to the curl of $\mathbf{v}$ being 0 everywhere, i.e. there are no regions of the tissue where the vector field $\mathbf{v}$ "rotates".

Second, we model each spatial domain R_p as a union of level sets of the isodepth d. Specifically, we assume that each spatial domain $R_p = \{(x, y) : b_{p-1} < d(x, y) \leq b_p\}$ is equal to the set of spatial locations (x, y) with isodepth $d(x, y)$ in the interval $(b_{p-1}, b_p]$, for some real numbers $-\infty = b_0 < b_1 < \cdots < b_{P-1} < b_P = \infty$. This ensures that the spatial domains R_p do not intersect, and leads to a particularly simple form for the expression function f_g as we show below.

Third, we assume that the scalar functions $\beta_g(x, y)$ are constant inside each spatial domain R_p; i.e., the scalar functions $\beta_g(x, y) = \sum_{p=1}^{P} \beta_{g,p} 1_{\{(x,y)\in R_p\}}$ are piecewise constant.

Under these assumptions, the spatial gradients ∇f_g in (4) are equal to

$$\nabla f_g(x, y) = \sum_{p=1}^{P} \beta_{g,p} \cdot \nabla d(x, y) \cdot 1_{\{b_{p-1}<d(x,y)\leq b_p\}}. \tag{5}$$

Integrating both sides of (5) yields the following closed form for the gene expression function f_g:

$$f_g(x, y) = \sum_{p=1}^{P} (\alpha_{g,p} + \beta_{g,p} \cdot d(x, y)) \cdot 1_{\{b_{p-1}<d(x,y)\leq b_p\}}, \tag{6}$$

for some constants $\alpha_{g,p}$ and $\beta_{g,p}$. Combining (6) for all genes $g = 1, \ldots, G$ yields the following expression for the gene expression vector $\mathbf{f} = (f_1, \ldots, f_G)$:

$$\mathbf{f}(x, y) = \sum_{p=1}^{P} (\boldsymbol{\alpha}_p + \boldsymbol{\beta}_p \cdot d(x, y)) \cdot 1_{\{b_{p-1}<d(x,y)\leq b_p\}}, \tag{7}$$

for vectors $\alpha_p = (\alpha_{g,p})_{g\in G} \in \mathbb{R}^G$ and $\beta_p = (\beta_{g,p})_{g\in G} \in \mathbb{R}^G$.

Thus, under our model, the gene expression function $\mathbf{f}(x, y)$ at spatial location $(x, y) \in T$ is given by the composition $\mathbf{f}(x, y) = \mathbf{h}(d(x, y))$ of the isodepth d and a *piecewise linear* function $\mathbf{h} = (h_1, \ldots, h_G) : \mathbb{R} \to \mathbb{R}^G$ with P pieces and breakpoints $b_1, \ldots, b_{P-1}$:

$$\mathbf{h}(w) = \sum_{p=1}^{P} (\boldsymbol{\alpha}_p + \boldsymbol{\beta}_p w) \cdot 1_{\{b_{p-1}<w\leq b_p\}}. \tag{8}$$

The vectors $\boldsymbol{\alpha}_p$ and $\boldsymbol{\beta}_p$ are the y-intercepts and slopes, respectively, of the function $\mathbf{h}$ in the p-th piece across all G genes. We call the function $\mathbf{h}(w)$ a *one-dimensional (1-D)* expression function as it is a function of a single variable w, the isodepth, in contrast to the gene expression function $\mathbf{f}(x, y)$ which is a function of two spatial variables x and y.

bioRxiv preprint doi: https://doi.org/10.1101/2023.10.10.561757; this version posted October 13, 2023. The copyright holder for this preprint (which was not certified by peer review) is the author/funder, who has granted bioRxiv a license to display the preprint in perpetuity. It is made available under aCC-BY-NC-ND 4.0 International license.

Long-range spatial correlations and pooling. A major advantage of modeling gene expression as a function of isodepth is the ability to combine gene expression measurements from distinct spatial locations and thus overcome the sparsity of current SRT technologies. Specifically, all spatial locations with equal isodepth d have identical gene expression value $\mathbf{h}(d)$, and so estimation of $\mathbf{h}(d)$ can use all locations on the contour of equal isodepth. This contour may traverse the entire tissue slice, and need not be a contiguous curve (e.g. Figure 2A). Thus, the isodepth model incorporates *"long-range"* spatial correlations [101], in contrast to many existing algorithms for analyzing SRT data which only incorporate local correlations between nearby spots, e.g. using hidden Markov random fields (HMRFs) [168, 34] or Gaussian processes (GPs) [135, 132, 130, 171]. Moreover, the isodepth model allows for "pooling" information across spatially separated regions of a tissue slice.

The isodepth model substantially generalizes the model of layered tissues and *"relative depth"* in [83] which restricted the spatial domains $R_1, \ldots, R_P$ to be layers satisfying strict topological constraints. In contrast, here there are fewer topological constraints on the spatial domains $R_1, \ldots, R_P$, and we learn the spatial domains and isodepth *de novo* from SRT data without any prior knowledge, as detailed below.

4.3 Maximum likelihood estimation

We compute the maximum likelihood estimators (MLEs) of the isodepth d and piecewise linear 1-D expression function $\mathbf{h} = (h_1, \ldots, h_G)$ from SRT data. The observed SRT data consists of a transcript count matrix $\mathbf{A} = [a_{i,g}] \in \mathbb{R}^{N \times G}$, where $a_{i,g}$ is the UMI count of gene g in spot i, and a spatial location matrix $\mathbf{S} \in \mathbb{R}^{N \times 2}$, where each row $\mathbf{s}_i = (x_i, y_i) \in \mathbb{R}^2$ is the spatial location of the i-th spot. We define the Spatial Topography Problem (STP) as the following maximum likelihood estimation problem.

Spatial Topography Problem (STP). *Given SRT data* $(\mathbf{A}, \mathbf{S})$ *and a number* P *of spatial domains, find a continuously differentiable function* $d : \mathbb{R}^2 \to \mathbb{R}$ *and a piecewise linear function* $\mathbf{h}(w) : \mathbb{R} \to \mathbb{R}^G$ *with* P *pieces that maximize the log-likelihood of the data:*

$$\underset{\substack{d \in C^1(\mathbb{R}^2, \mathbb{R}) \\ b_1 < b_2 < \cdots < b_{P-1} \\ \mathbf{h} = (h_1, \ldots, h_G) \in \mathcal{L}(b_1, \ldots, b_{P-1})}}{\operatorname{argmax}} \quad \sum_{g=1}^{G} \left(\sum_{i=1}^{N} \log \mathbb{P}\Big(a_{i,g} \mid h_g\big(d(x_i, y_i)\big) \Big) \right), \tag{9}$$

where $C^1(\mathbb{R}^2, \mathbb{R})$ *is the space of continuously differentiable functions from* $\mathbb{R}^2$ *to* $\mathbb{R}$ *and* $\mathcal{L}(b_1, \ldots, b_{P-1})$ *is the set of piecewise linear functions with breakpoints* $b_1, \ldots, b_{P-1}$.

The STP substantially generalizes the L-Layered Problem from our previous work [83], which assumed the isodepth d was given by a piecewise conformal map where the pieces are either bounded by lines or determined by prior knowledge on the shape of the spatial domains R_p.

The STP is a challenging non-convex optimization problem over spaces of continuously differentiable and piecewise continuous functions. We solve this optimization problem using *deep learning*. By the universal approximation theorem [56], one can approximate a continuous function d with a neural network. Moreover, even a *piecewise* continuous function can be well-approximated by neural networks [79], although it may be computationally intractable to identify the individual pieces of the function [123]. Thus, we solve the STP in a two-step approach, where we first learn the isodepth d and then learn the piecewise linear expression function $\mathbf{h}$.

Step 1. We estimate the isodepth d by solving a modified version of the maximum likelihood problem in (9) where we parametrize the functions $d : \mathbb{R}^2 \to \mathbb{R}$ and $\mathbf{h} = (h_1, \ldots, h_G) : \mathbb{R} \to \mathbb{R}^G$ with neural networks with weights θ and θ', respectively.

bioRxiv preprint doi: https://doi.org/10.1101/2023.10.10.561757; this version posted October 13, 2023. The copyright holder for this preprint (which was not certified by peer review) is the author/funder, who has granted bioRxiv a license to display the preprint in perpetuity. It is made available under aCC-BY-NC-ND 4.0 International license.

$$\underset{\theta,\theta'}{\operatorname{argmax}} \quad \sum_{g=1}^{G}\left(\sum_{i=1}^{N}\log \mathbb{P}\Big(a_{i,g} \mid \mathbf{h}_{\theta'}\big(d_\theta(x_i,y_i)\big)_g\Big)\right). \tag{10}$$

The modified problem in (10) is also a non-convex optimization problem for most neural network architectures. Nevertheless, by parametrizing the arguments with neural networks, we leverage the fact that such problems can be approximately and efficiently solved by modern deep learning frameworks such as PyTorch [102].

Solving (10) is equivalent to learning the parameters of a *single* neural network $\mathbf{h}_{\theta'} \circ d_\theta$, where one of the hidden layers has only one hidden neuron whose value is the estimated isodepth d_θ (Figure 1). As a result, the isodepth corresponds to an *interpretable* hidden layer of a neural network.

Using the solution $\widehat{\theta}$ from (10) yields an estimate $\widehat{d} = d_{\widehat{\theta}}$ of the isodepth d. We expect the estimated isodepth $\widehat{d}$ to be a good approximation of the solution to the STP (9), as both continuous functions d and piecewise continuous functions $\mathbf{h}$ can be well-approximated by neural networks [79]. However, it is difficult to identify the breakpoints $b_1, \ldots, b_{P-1}$ — and thus the spatial domains R_p of the tissue slice — from the neural network $\mathbf{h}_{\theta'}$. Therefore, we solve a second optimization problem to estimate the piecewise linear function $\mathbf{h}$.

Step 2. We use the estimated isodepth $\widehat{d}$ from Step 1 to estimate the piecewise linear function $\widehat{\mathbf{h}}$ with breakpoints $\widehat{b}_1, \ldots, \widehat{b}_p$ by solving the following optimization problem:

$$\underset{\substack{b_1<b_2<\cdots<b_{P-1}\\ \mathbf{h}=(h_1,\ldots,h_G)\in\mathcal{L}(b_1,\ldots,b_{P-1})}}{\operatorname{argmax}} \quad \sum_{g=1}^{G}\left(\sum_{i=1}^{N}\log \mathbb{P}\Big(a_{i,g} \mid h_g\big(\widehat{d}(x_i,y_i)\big)\Big)\right). \tag{11}$$

When there is only one gene, i.e. $G = 1$, then the maximum likelihood problem in (11) is an instance of segmented regression, a classical problem from statistics that is solved by dynamic programming (DP) [3, 7]. For $G > 1$ genes, we solve (11) using a variant of the segmented regression DP derived in [83].

4.4 Training and implementation

The algorithm described above can be implemented with different probability distributions $\mathbb{P}(a_{i,g} \mid f_g(x_i,y_i)) = \mathbb{P}(a_{i,g} \mid h_g(d(x_i,y_i)))$ for the gene expression values $a_{i,g}$. Following prior work [136, 120, 83, 100], we model the UMI counts $a_{i,g}$ with a Poisson distribution of the form $a_{i,g} \overset{\text{i.i.d.}}{\sim} \text{Pois}\Big(U_i \cdot \exp\big(f_g(x_i,y_i)\big)\Big)$, where U_i is the total UMI count at spot i. Another alternative is a Gaussian measurement model $a_{i,g} \overset{\text{i.i.d.}}{\sim} N(f_g(x_i,y_i),\sigma^2)$ where σ^2 is a shared variance parameter.

In practice, although one could use all or selected gene expression values instead, for efficiency we do not directly solve the STP (9) using the observed gene expression values but instead use the top generalized linear model principal components (GLM-PCs) [136]. This simplification is justified by our previous work [83] where we showed that for SRT data $(\mathbf{A}, \mathbf{S})$ generated from the Poisson expression model with a piecewise linear expression function $\mathbf{h}$, then the top-$2P$ GLM-PCs of the transcript count matrix $\mathbf{A}$ are also piecewise linear with Gaussian noise.

Specifically, we compute the top-$2P$ GLM-PCs and solve (10) with these GLM-PCs under a Gaussian error model. For the colorectal tumor (Section 2.4), in order to capture spatial variation from the histological image, we use the top-$(2P-3)$ GLM-PCs together with the mean R, G, and B values taken from the H&E stained image, resulting in $(2P-3)+3 = 2P$ total features in the STP. We solve the optimization problem in (10) with neural networks d_θ and $\mathbf{h}_{\theta'}$ that have two hidden layers of size 20 and are trained

bioRxiv preprint doi: https://doi.org/10.1101/2023.10.10.561757; this version posted October 13, 2023. The copyright holder for this preprint (which was not certified by peer review) is the author/funder, who has granted bioRxiv a license to display the preprint in perpetuity. It is made available under aCC-BY-NC-ND 4.0 International license.

for 10000 epochs using the Adam optimizer [66]. Because of the non-convexity of (10), we use 30 random initializations and select the solution with the largest likelihood.

After solving (10) with the top-$2P$ GLM-PCs and estimating the isodepth $\widehat{d}$, we then solve (11) with the top GLM-PCs to estimate the breakpoints $\widehat{b}_1, \ldots, \widehat{b}_{P-1}$. For most of the applications in this paper, we choose the number P of spatial domains using prior knowledge on the geometry of the tissue slice, e.g. for the cerebellum (Figure 2), we use $P = 4$ as prior work [19] showed that the cerebellum has four distinct layers. However, if the number P of domains is not known, then one may follow the model selection criteria used by [83], i.e. identifying an elbow in the log-likelihood plot, which we use for the DLPFC application (Figure S3).

Finally, we estimate the piecewise linear gene expression function $\widehat{\mathbf{h}}$ by solving

$$\underset{\mathbf{h}=(h_1,\ldots,h_G)\in\mathcal{L}(\widehat{b}_1,\ldots,\widehat{b}_{P-1})}{\operatorname{argmax}} \sum_{g=1}^{G}\left(\sum_{i=1}^{N}\log\mathbb{P}\Big(a_{i,g}\mid h_g\big(\widehat{d}(x_i,y_i)\big)\Big)\right) \tag{12}$$

under the Poisson expression model for the UMI counts $a_{i,g}$. We solve the optimization problem in (12) using Poisson regression with `sklearn` [103] for each individual gene g and spatial domain R_p. To prevent overfitting, we subsequently perform a hypothesis test of whether each slope $\beta_{g,p}$ of gene g in domain R_p is zero or non-zero, i.e. we test the hypotheses

$$H_0 : \beta_{g,p} = 0 \tag{13}$$

$$H_1 : \beta_{g,p} \neq 0. \tag{14}$$

For each gene g and domain R_p, we compute a log-likelihood ratio (LLR) for the null and alternative hypotheses under the Poisson expression model, and we estimate a p-value assuming that $2 \cdot \text{LLR}$ follows a χ^2-distribution, which holds asymptotically by Wilks' theorem [147]. We set the slope $\beta_{g,p}$ to zero if the p-value is less than 0.1.

Moreover, we estimate a 1-D expression function h_g only for genes g with at least K total UMI counts where $K = 500$ for the cerebellum and olfactory bulb (Sections 2.3, 2.5) and $K = 1000$ for the colorectal tumor (Section 2.4). These choices of K result in $\approx 2000 - 5000$ genes for which we estimate an expression function. Moreover, for Slide-SeqV2 and Stereo-Seq applications with sparse UMI counts, we only estimate a slope $\beta_{g,p}$ in domain R_p if there are at least T non-zero expression values in the domain. We use $T = 75$ for the cerebellum and $T = 20$ for the olfactory bulb, which are approximately 10% of the number of spatial locations in the smallest domain.

4.5 Quantifying spatial variation in gene expression

The piecewise linear expression functions $h_g(w) = \sum_{p=1}^{P}(\alpha_p + \beta_p) \cdot 1_{\{b_{p-1} < w \leq b_p\}}$ reveal both discontinuities in expression and continuous variation within a domain, or intradomain variation, as we describe below.

Discontinuous expression. Let $\delta_{g,p}$ be the discontinuity of the function h_g at breakpoint b_p, i.e. $\delta_{g,p} = (\alpha_{g,p+1} + \beta_{g,p+1} \cdot b_p) - (\alpha_{g,p} + \beta_{g,p} \cdot b_p)$. A large (absolute) discontinuity $|\delta_{g,p}|$ indicates a large discontinuous change in the expression of gene g at the boundary between spatial domains R_p and R_{p+1}.

We say a gene g has a *discontinuity* in expression between spatial domains R_p and R_{p+1} if the estimated discontinuity magnitude $|\widehat{\delta}_{g,p}|$ is greater than a threshold t_p. We set the threshold t_p to be the tenth percentile of all estimated discontinuity magnitudes $\left(|\widehat{\delta}_{g,p}|\right)_{g=1,\ldots,G}$ between spatial domains R_p and R_{p+1}.

bioRxiv preprint doi: https://doi.org/10.1101/2023.10.10.561757; this version posted October 13, 2023. The copyright holder for this preprint (which was not certified by peer review) is the author/funder, who has granted bioRxiv a license to display the preprint in perpetuity. It is made available under aCC-BY-NC-ND 4.0 International license.

Intradomain variation. The slope $\beta_{g,p}$ of the expression function h_g describes variation within a spatial domain R_p. We say a gene g has *intradomain variation* in spatial domain R_p if the estimated magnitude $|\widehat{\beta}_{g,p}|$ of the slope is greater than a threshold s_p. That is, intradomain variation corresponds to a large *effect size* of the parameter $\beta_{g,p}$. (Note that this effect size thresholding is distinct from the p-value thresholding in Section 4.4.) We set the threshold s_p to be the tenth percentile of all estimated slope magnitudes $\left(|\widehat{\beta}_{g,p}|\right)_{g=1,\ldots,G}$ in domain R_p.

4.6 Attributing continuous variation in expression to cell types

Intradomain variation in expression – i.e. a large magnitude of the slope $\beta_{g,p}$ for a domain R_p in the piecewise linear fit – may be due to variation in expression within a cell type, variation in the proportions of cell types, or other biological causes. To illustrate, consider the 1-D expression function $h(w) = h_g(w)$ for a single gene g. Given cell types $c = 1, \ldots, C$, the function $h(w)$ is given by

$$h(w) = \sum_{c=1}^{C} \big(h_c(w) \cdot u_c(w)\big) + \epsilon(w) \tag{15}$$

where $h_c : \mathbb{R} \to \mathbb{R}$ is the *cell type c-specific* expression, $0 \leq u_c(w) \leq 1$ is the proportion of cell type c at isodepth w, and $\epsilon(w)$ represents variation due to other factors.

Suppose that the expression function is $h(w) = e \cdot u_c(w) + \epsilon(w)$; i.e. expression is constant for cell type c and zero for other cell types. If the cell type proportion $u_c(w)$ or other variation function $\epsilon(w)$ are not constant functions of the isodepth w, then the function $h(w)$ will not be constant. Thus, when we fit the expression function $h(w)$ with a piecewise linear function, we may estimate a non-zero slope β — reflecting variation in expression — even when there is no variation for any given cell type. This motivates the problem of learning *cell type-specific* expression functions $h_{c,g} : \mathbb{R} \to \mathbb{R}$ for each gene g and cell type c which reveal whether variation is attributable to cell type or to other factors.

Here we derive a simple approach for estimating cell type-specific expression functions $h_{c,g}$ from *single-cell resolution* SRT data with cell type annotations. Specifically, suppose we are given single-cell resolution SRT data $(\mathbf{A}, \mathbf{S})$ with cell type annotations $z_{i,c} \in \{0, 1\}$, where $z_{i,c} = 1$ if spot i contains cell type c, and $z_{i,c} = 0$ otherwise. We assume the isodepth d and breakpoints $b_1, \ldots, b_{P-1}$ have already been computed as described in Section 4.4. We model the expression $a_{i,g}$ at spatial location (x_i, y_i) with the Poisson expression model $a_{i,g} \sim \text{Pois}\left(U_i \cdot \exp\left(\sum_{c=1}^{C} z_{i,c} h_{c,g}(d(x_i, y_i))\right)\right)$ where U_i is the total UMI count at spatial location (x_i, y_i). Similar to Section 4.2, we model the cell type-specific expression functions $\mathbf{h}_c = (h_{c,1}, \ldots, h_{c,G}) : \mathbb{R} \to \mathbb{R}^G$ as piecewise linear functions of the form

$$\mathbf{h}_c(w) = \sum_{p=1}^{P} (\boldsymbol{\alpha}_{c,p} + \boldsymbol{\beta}_{c,p} w) \cdot 1_{\{b_{p-1} < w \leq b_p\}}. \tag{16}$$

where $\boldsymbol{\alpha}_{c,p} = (\alpha_{c,p,g})_{g=1,\ldots,G}$ and $\boldsymbol{\beta}_{c,p} = (\beta_{c,p,g})_{g=1,\ldots,G}$ are the *cell type c-specific* y-intercepts and slopes, respectively, of the *cell type c-specific* expression function $\mathbf{h}_c = (h_{c,1}, \ldots, h_{c,G})$ in spatial domain R_p.

The MLE of the piecewise linear, cell type c-specific expression functions $\mathbf{h}_c = (h_{c,g})_{g \in G}$ is given by

$$\max_{\mathbf{h}_1, \ldots, \mathbf{h}_C \in \mathcal{L}(\widehat{b}_1, \ldots, \widehat{b}_{P-1})} \sum_{c=1}^{C} \sum_{g=1}^{G} \left(\sum_{i=1}^{N} \log \mathbb{P}\Big(a_{i,g} \mid h_{c,g}, z_{i,c}\Big) \right) = \sum_{c=1}^{C} \left[\max_{\mathbf{h}_c \in \mathcal{L}(\widehat{b}_1, \ldots, \widehat{b}_{P-1})} \sum_{g=1}^{G} \left(\sum_{i : z_{i,c}=1} \log \mathbb{P}\Big(a_{i,g} \mid h_{c,g}\Big) \right) \right]. \tag{17}$$

The inner optimization problem is an instance of the optimization problem in (12) restricted to spots i with cell type c, i.e. $z_{i,c} = 1$, and is solved using the same Poisson regression approach. Solving (17) yields

bioRxiv preprint doi: https://doi.org/10.1101/2023.10.10.561757; this version posted October 13, 2023. The copyright holder for this preprint (which was not certified by peer review) is the author/funder, who has granted bioRxiv a license to display the preprint in perpetuity. It is made available under aCC-BY-NC-ND 4.0 International license.

estimated piecewise linear functions $\widehat{h}_{c,g}$ with y-intercept $\widehat{\alpha}_{c,p,g}$ and slope $\widehat{\beta}_{c,p,g}$ for each gene g in domain R_p and cell type c.

To assess whether intradomain variation is attributable to cell type, we compare the cell type c-specific slope $\beta_{c,g,p}$ to the *cell type-agnostic* slope $\beta_{g,p}$, which is derived from the *cell type-agnostic* expression function $\mathbf{h}(w)$ (Equation (8)). Specifically, we refer to the parameters $\boldsymbol{\alpha}_p = (\alpha_{g,p})_{g\in G}$ and $\boldsymbol{\beta}_p = (\beta_{g,p})_{g\in G}$ as the *cell type-agnostic* y-intercepts and slopes, respectively. If the cell type c-specific slope $\beta_{c,g,p}$ is close or larger in magnitude to the *cell type-agnostic* slope $\beta_{g,p}$, then the continuous variation in expression — i.e. the large value of $\beta_{g,p}$ — is attributed to cell type c. Conversely, if the cell type-specific slope $\beta_{c,g,p}$ is much smaller in magnitude than the cell type-agnostic slope $\beta_{g,p}$, then the continuous variation in expression is not attributable to cell type c.

We quantify this intuition by dividing the genes with continuous variation identified in Section 4.5 into two groups based on the estimated cell type-specific slopes $\widehat{\beta}_{c,g,p}$. If $|\widehat{\beta}_{c,g,p}| > (1-\gamma)|\widehat{\beta}_{g,p}|$ for some cell type c and a fixed constant γ, i.e. the magnitude of the cell type-specific slope $\widehat{\beta}_{c,g,p}$ is close to or larger than the magnitude of the slope $\widehat{\beta}_{g,p}$, then we say that the expression variation within domain R_p is *attributable to cell type* c. On the other hand, if $|\widehat{\beta}_{c,g,p}| \leq (1-\gamma)|\widehat{\beta}_{g,p}|$ for all cell types c, then we say that there is *other* variation in the expression of gene g within domain R_p. We use $\gamma = 0.5$ in our analyses.

4.7 Visualization

4.7.1 Scaling isodepth to physical distance

The neural network in GASTON learns an isodepth $d(x, y)$ that smoothly varies across a tissue slice T; however, the scaling of the learned isodepth $d(x, y)$ is arbitrary. To improve the interpretability of the isodepth $d(x, y)$ learned by the neural network, we scale the isodepth in each spatial domain to reflect approximate physical distances inside the domain. Briefly, we derive an estimate γ_p of the "average width" of each spatial domain R_p in μm, and we linearly transform the isodepth $d(x, y)$ in each spatial domain such that the range of isodepth values in domain R_P is γ_p.

We scale the isodepth in each spatial domain as follows. Given the isodepth $d(x, y)$, spatial domains $R_1, \ldots, R_P$, and breakpoints $b_1, \ldots, b_{P-1}$ estimated from (10) and (11), we assume without loss of generality that the isodepth is linearly transformed such that $\min_{(x,y)\in T} d(x, y) = 0$ and $\max_{(x,y)\in T} d(x, y) = 1$, i.e. the breakpoints satisfy $b_0 = 0 < b_1 < \cdots < b_{P-1} < 1 = b_P$, where we set $b_0 = 0$ and $b_P = 1$ for convenience. For each spatial domain R_p, let γ_p be the average width of the domain, whose computation we describe below. We compute the *"scaled"* isodepth $\widetilde{d}(x, y)$ as

$$\widetilde{d}(x, y) = \sum_{p=1}^{P} \left(e_p + f_p \cdot d(x, y)\right) \cdot 1_{\{b_{p-1} < d(x,y) \leq b_p\}}, \tag{18}$$

where e_p, f_p are chosen such that $\widetilde{d}(x, y)$ is continuous, and $\widetilde{d}(x, y) = \sum_{q=1}^{p} \gamma_q$ if $d(x, y) = b_p$ for $p = 1, \ldots, P$. With this choice of e_p, f_p, the range of scaled isodepth values $\widetilde{d}(x, y)$ in a spatial domain R_p is given by

$$\max_{(x,y)\in R_p} \widetilde{d}(x, y) - \min_{(x,y)\in R_p} \widetilde{d}(x, y) = \max_{b_{p-1} < d(x,y) \leq b_p} \widetilde{d}(x, y) - \min_{b_{p-1} < d(x,y) \leq b_p} \widetilde{d}(x, y) = \sum_{q=1}^{p} \gamma_q - \sum_{q=1}^{p-1} \gamma_q = \gamma_p. \tag{19}$$

That is, the range of isodepth values $\widetilde{d}(x, y)$ in each spatial domain is the average width γ_p of the domain R_p.

We estimate the average width γ_p of each spatial domain R_p by computing the median physical distance between the two boundaries of the domain R_p. Specifically, let $\Gamma_{\text{lower}} = \{(x_i, y_i) \in R_p : b_{p-1} < d(x_i, y_i) <$

bioRxiv preprint doi: https://doi.org/10.1101/2023.10.10.561757; this version posted October 13, 2023. The copyright holder for this preprint (which was not certified by peer review) is the author/funder, who has granted bioRxiv a license to display the preprint in perpetuity. It is made available under aCC-BY-NC-ND 4.0 International license.

$b_{p-1}+\epsilon\}$ and let $\Gamma_{\text{upper}} = \{(x_i, y_i) \in R_p : b_p - \epsilon' < d(x_i, y_i) < b_p\}$ be the set of spatial locations on the lower and upper boundary curves of the spatial domain R_p, respectively. We set γ_p to be the median distance between each spot $(x, y) \in \Gamma_{\text{lower}}$ and the closest spot in Γ_{upper} We choose ϵ, ϵ' such that Γ_{lower} and Γ_{upper} visually correspond to the spatial domain boundaries.

For 10x Genomics Visium data, we multiply each average width γ_p by 100, since the physical distance between the centers of adjacent spots in the 10x Visium slide is 100μm. For Slide-seqV2 data, we multiply each average width γ_p by 64/100, since two beads that are 100 pixels apart in the Slide-SeqV2 microscopy image have a physical distance of roughly 64μm [116].

4.7.2 Visualizing 1-D expression functions

To simplify the visualization of the 1-D expression functions $\mathbf{h}$, we aggregate the counts $a_{i,g}$ for spots (x_i, y_i) with approximately equal isodepth values $d(x_i, y_i)$, as in [83]. Specifically, we partition the range of isodepth values into a union $B_1 \cup \cdots \cup B_M$ of intervals B_j, and we compute the total expression value $\widetilde{a}_{j,g} = \sum_{i:d(x_i,y_i)\in B_j} a_{i,g}$ for gene g in each interval B_j. We call $\widetilde{a}_{j,g}$ the *pooled* expression value of gene g at pooled spot j. Pooling does not affect inference of the 1-D expression function $\mathbf{h}$ in the STP, as the function $\mathbf{h}$ obtained by maximizing the log-likelihood (9) with pooled data is equal to the function obtained by maximizing (9) with the original data, as shown in [83].

We plot expression as log pooled counts per million (CPM) $\log(\widetilde{a}_{j,g}/\widetilde{D}_j \cdot 10^6 + 1)$, where $\widetilde{D}_j$ is the sum of the total UMI counts across all spots in the jth pooled spot. The log pooled CPM has approximately the same scale as the expression function $h_g(w) + \log(10^6)$ for each gene g.

4.8 Marker gene analysis

For the marker gene comparison in Section 2.3, we derived a ranking of domain specific marker genes from the GASTON inferred 1-D expression functions h_g by ranking genes by the standard deviation of the mean of each expression function. Specifically, for each gene g, we compute the mean $m_{g,p}$ of the 1-D expression function $h_g(w)$ in spatial domain R_p, i.e. $m_{g,p} = \alpha_p + \beta_p \cdot \left(\frac{b_{p-1}+b_p}{2}\right)$, and we rank genes by the standard deviation of the values $(m_{g,p})_{p=1,\ldots,P}$. Intuitively, a marker gene should have high expression in one spatial domain and low expression in other domains, leading to a large standard deviation, while a non-marker gene will have similar expression in all domains, leading to a small standard deviation.

4.9 Spatial coherence score

We quantify the spatial coherence of domain labels using a score based on O'Neill's spatial entropy measure [98, 4] which has previously been used to quantify spatial coherence in SRT data [159]. The spatial entropy measures the fraction of neighboring spots having the same label compared to random assignments of labels. A large spatial entropy indicates that the distribution of labels of neighboring spots is close to the uniform distribution, i.e the labels are spatially coherent, whereas a small spatial entropy indicates that nearby spots frequently have the same label, i.e. the labels are spatially coherent.

We use a modified version of the spatial coherence score used by [159] that is scaled to lie in $[0, 1]$. Specifically, following the notation in [159], we define the spatial coherence score as $C_G(L) = 1 - \frac{H(G,L)}{\log(k(k+1)/2)}$.

4.10 Data collection and method details

For the cerebellum analysis in Sections 2.2 and 2.3, we used replicate 1 from the RCTD/C-SIDE data repository [18]. Figure 2J was created with `BioRender.com`. For the marker gene comparison in Figure 3A, we derived a gene ranking for each method and evaluated the AUPRC compared to known marker genes of the

bioRxiv preprint doi: https://doi.org/10.1101/2023.10.10.561757; this version posted October 13, 2023. The copyright holder for this preprint (which was not certified by peer review) is the author/funder, who has granted bioRxiv a license to display the preprint in perpetuity. It is made available under aCC-BY-NC-ND 4.0 International license.

oligodendrocyte, granule, Purkinje, Bergmann, and molecular cell types in the cerebellum. These marker genes were the combination of cell type marker genes from PanglaoDB [40], the Allen Mouse Brain Atlas [71], Harmonizome [118], and the supplement of [69].

We obtained the olfactory bulb SRT dataset from [42]. We obtained cell type annotations for each spot in the tissue (Figure 5D) by using scANVI [154] to integrate the SRT data with a separate mouse olfactory bulb scRNA-seq dataset [133]; for the scRNA-seq data, we followed the pre-processing steps in [76].

SpiceMix. We followed the Visium Jupyter notebook tutorial on Github with parameters $K = 6$ (for the K-NN graph) and `n_neighbors=200`.

Non-negative spatial factorization (NSF). We followed the Github tutorial and trained for 150 iterations to obtain 10 factors. Since NSF identifies factors rather than spatial domains, we identified NSF spatial domains by using the NSF factors as input for the Louvain clustering module from SpiceMix [24].

RCTD/C-SIDE. For the cerebellum analysis, we used the cell type labels provided in the RCTD data repository. We followed the C-SIDE tutorial to identify cell type-specific differentially expressed genes. We ran two versions of C-SIDE: (1) without any covariates, and (2) with the isodepth $d(x, y)$ as a covariate for each spatial location (x, y). For the analysis in Section 2.3, we ranked genes by their minimum C-SIDE p-value across all cell types.

SpaGCN. We ran SpaGCN following the Github tutorial. For the analysis in Section 2.3, we used a ranking where the SpaGCN spatially varying genes are tied for first and all other genes are tied for second.

HotSpot. We ran HotSpot following the tutorial here. For the analysis in Section 2.3, we ranked genes according to their p-value.

trendsceek*. We used the Seurat implementation of trendsceek as described here. For the analysis in Section 2.3, we ranked genes according to their p-value.

SpatialDE. We ran SpatialDE following the Github example. For the analysis in Section 2.3 we ranked genes according to their p-value.

SPARK-X. We ran Spark-X following the tutorial here. For the analysis in Section 2.3 we ranked genes according to their p-value.

SpaceFold. We ran SpaceFold following the Github example code.

Acknowledgements

This research is supported by National Cancer Institute (NCI) grants U24CA248453 and U24CA264027 to B.J.R. U.C. was supported by a National Science Foundation Graduate Research Fellowship and the Siebel Scholars program. B.J.A. gratefully acknowledges financial support from the Schmidt DataX Fund at Princeton University, made possible through a major gift from the Schmidt Futures Foundation. H.S. is funded by the Princeton Ludwig Branch. C.M. is a Damon Runyon Fellow supported by the Damon Runyon Cancer Research Foundation (DRQ-15-22).

bioRxiv preprint doi: https://doi.org/10.1101/2023.10.10.561757; this version posted October 13, 2023. The copyright holder for this preprint (which was not certified by peer review) is the author/funder, who has granted bioRxiv a license to display the preprint in perpetuity. It is made available under aCC-BY-NC-ND 4.0 International license.

Data and code availability

This paper analyzes existing, publicly available data. The cerebellum SRT dataset was obtained from [18]; the olfactory bulb SRT data set was obtained from [42]; the colorectal tumor SRT dataset was obtained from [149]; and the DLPFC SRT dataset was obtained from [89]. The code for GASTON is publicly available at https://github.com/raphael-group/GASTON.

References

[1] 10x Visium Genomics Visium Spatial Gene Expression. https://www.10xgenomics.com/products/spatial-gene-expression.

[2] Expression patterns of hypoxic markers at the invasive margin of colorectal cancers and liver metastases. *European Journal of Surgical Oncology*, 35:1286–1294, 2009.

[3] J. Acharya, I. Diakonikolas, J. Li, and L. Schmidt. Fast algorithms for segmented regression. In *International Conference on Machine Learning*, pages 2878–2886. PMLR, 2016.

[4] L. Altieri, D. Cocchi, and G. Roli. Spatentropy: Spatial entropy measures in r. *arXiv preprint arXiv:1804.05521*, 2018.

[5] G. Amore, G. Spoto, A. Ieni, L. Vetri, G. Quatrosi, G. Di Rosa, and A. G. Nicotera. A focus on the cerebellum: From embryogenesis to an age-related clinical perspective. *Frontiers in Systems Neuroscience*, 15:646052, 2021.

[6] H. L. Ashe and J. Briscoe. The interpretation of morphogen gradients. 2006.

[7] J. Bai and P. Perron. Estimating and testing linear models with multiple structural changes. *Econometrica*, pages 47–78, 1998.

[8] J. Barker, T. Behar, Y. Li, Q. Liu, W. Ma, D. Maric, I. Maric, A. Schaffner, R. Serafini, S. Smith, et al. Gabaergic cells and signals in cns development. *Perspectives on developmental neurobiology*, 5(2-3):305–322, 1998.

[9] S. Ben-Moshe and S. Itzkovitz. Spatial heterogeneity in the mammalian liver. *Nature reviews Gastroenterology & hepatology*, 16(7):395–410, 2019.

[10] F. M. Benes and S. Berretta. Gabaergic interneurons: implications for understanding schizophrenia and bipolar disorder. *Neuropsychopharmacology*, 25(1):1–27, 2001.

[11] V. Bergen, R. A. Soldatov, P. V. Kharchenko, and F. J. Theis. Rna velocity—current challenges and future perspectives. *Molecular systems biology*, 17(8):e10282, 2021.

[12] E. Berglund, J. Maaskola, N. Schultz, S. Friedrich, M. Marklund, J. Bergenstråhle, F. Tarish, A. Tanoglidi, S. Vickovic, L. Larsson, et al. Spatial maps of prostate cancer transcriptomes reveal an unexplored landscape of heterogeneity. *Nature communications*, 9(1):2419, 2018.

[13] R. Blazeski, C. A. Mason, et al. Cell-cell interactions influence survival and differentiation of purified purkinje cells in vitro. *Neuron*, 12(2):243–260, 1994.

[14] B. P. Blum and J. J. Mann. The gabaergic system in schizophrenia. *International Journal of Neuropsychopharmacology*, 5(2):159–179, 2002.

bioRxiv preprint doi: https://doi.org/10.1101/2023.10.10.561757; this version posted October 13, 2023. The copyright holder for this preprint (which was not certified by peer review) is the author/funder, who has granted bioRxiv a license to display the preprint in perpetuity. It is made available under aCC-BY-NC-ND 4.0 International license.

[15] D. G. Bonett. Confidence interval for a coefficient of quartile variation. *Computational statistics & data analysis*, 50(11):2953–2957, 2006.

[16] S. Bonin, A. Parascandolo, C. Aversa, R. Barbazza, N. Tsuchida, M. D. Castellone, G. Stanta, and G. Vecchio. Reduced expression of α-l-fucosidase-1 (fuca-1) predicts recurrence and shorter cancer specific survival in luminal b ln+ breast cancer patients. *Oncotarget*, 9(20):15228, 2018.

[17] A. Butler, P. Hoffman, P. Smibert, E. Papalexi, and R. Satija. Integrating single-cell transcriptomic data across different conditions, technologies, and species. *Nature Biotechnology*, 36:411–420, 2018.

[18] D. M. Cable, E. Murray, V. Shanmugam, S. Zhang, L. S. Zou, M. Diao, H. Chen, E. Z. Macosko, R. A. Irizarry, and F. Chen. Cell type-specific inference of differential expression in spatial transcriptomics. *Nature methods*, 19(9):1076–1087, 2022.

[19] D. M. Cable, E. Murray, L. S. Zou, A. Goeva, E. Z. Macosko, F. Chen, and R. A. Irizarry. Robust decomposition of cell type mixtures in spatial transcriptomics. *Nature biotechnology*, 40(4):517–526, 2022.

[20] A. Calon, E. Lonardo, A. Berenguer-Llergo, E. Espinet, X. Hernando-Momblona, M. Iglesias, M. Sevillano, S. Palomo-Ponce, D. V. Tauriello, D. Byrom, et al. Stromal gene expression defines poor-prognosis subtypes in colorectal cancer. *Nature genetics*, 47(4):320–329, 2015.

[21] M. S. Cembrowski, J. L. Bachman, L. Wang, K. Sugino, B. C. Shields, and N. Spruston. Spatial gene-expression gradients underlie prominent heterogeneity of ca1 pyramidal neurons. *Neuron*, 89(2):351–368, 2016.

[22] A. Chen, S. Liao, M. Cheng, K. Ma, L. Wu, Y. Lai, X. Qiu, J. Yang, J. Xu, S. Hao, et al. Spatiotemporal transcriptomic atlas of mouse organogenesis using dna nanoball-patterned arrays. *Cell*, 185(10):1777–1792, 2022.

[23] H. Chen, D. Li, and Z. Bar-Joseph. Cell segmentation for high-resolution spatial transcriptomics. In *Research in Computational Molecular Biology: 27th Annual International Conference, RECOMB 2023, Istanbul, Turkey, April 16–19, 2023, Proceedings*, volume 13976, page 251. Springer Nature, 2023.

[24] B. Chidester, T. Zhou, S. Alam, and J. Ma. Spicemix enables integrative single-cell spatial modeling of cell identity. *Nature Genetics*, 55(1):78–88, 2023.

[25] F. Clotman, P. Jacquemin, N. Plumb-Rudewiez, C. E. Pierreux, P. Van der Smissen, H. C. Dietz, P. J. Courtoy, G. G. Rousseau, and F. P. Lemaigre. Control of liver cell fate decision by a gradient of tgfβ signaling modulated by onecut transcription factors. *Genes & development*, 19(16):1849–1854, 2005.

[26] G. G. Consalez, D. Goldowitz, F. Casoni, and R. Hawkes. Origins, development, and compartmentation of the granule cells of the cerebellum. *Frontiers in neural circuits*, page 88, 2021.

[27] A. S. Cuomo, A. Nathan, S. Raychaudhuri, D. G. MacArthur, and J. E. Powell. Single-cell genomics meets human genetics. *Nature Reviews Genetics*, pages 1–15, 2023.

[28] X. Dai, L. Xiang, T. Li, and Z. Bai. Cancer hallmarks, biomarkers and breast cancer molecular subtypes. *Journal of cancer*, 7(10):1281, 2016.

[29] Z.-M. Dai, W. Guo, D. Yu, X.-J. Zhu, S. Sun, H. Huang, M. Jiang, B. Xie, Z. Zhang, and M. Qiu. Secisbp2l-mediated selenoprotein synthesis is essential for autonomous regulation of oligodendrocyte differentiation. *Journal of Neuroscience*, 42(30):5860–5869, 2022.

bioRxiv preprint doi: https://doi.org/10.1101/2023.10.10.561757; this version posted October 13, 2023. The copyright holder for this preprint (which was not certified by peer review) is the author/funder, who has granted bioRxiv a license to display the preprint in perpetuity. It is made available under aCC-BY-NC-ND 4.0 International license.

[30] A. Deshpande, M. Loth, D. N. Sidiropoulos, S. Zhang, L. Yuan, A. T. Bell, Q. Zhu, W. J. Ho, C. Santa-Maria, D. M. Gilkes, et al. Uncovering the spatial landscape of molecular interactions within the tumor microenvironment through latent spaces. *Cell Systems*, 14(4):285–301, 2023.

[31] D. DeTomaso and N. Yosef. Hotspot identifies informative gene modules across modalities of single-cell genomics. *Cell systems*, 12(5):446–456, 2021.

[32] K. Dong and S. Zhang. Deciphering spatial domains from spatially resolved transcriptomics with an adaptive graph attention auto-encoder. *Nature communications*, 13(1):1739, 2022.

[33] R. Doucette. Development of the nerve fiber layer in the olfactory bulb of mouse embryos. *Journal of Comparative Neurology*, 285(4):514–527, 1989.

[34] R. Dries, Q. Zhu, R. Dong, C.-H. L. Eng, H. Li, K. Liu, Y. Fu, T. Zhao, A. Sarkar, F. Bao, et al. Giotto: a toolbox for integrative analysis and visualization of spatial expression data. *Genome biology*, 22:1–31, 2021.

[35] D. Edsgärd, P. Johnsson, and R. Sandberg. Identification of spatial expression trends in single-cell gene expression data. *Nature methods*, 15(5):339–342, 2018.

[36] A. Erickson, M. He, E. Berglund, M. Marklund, R. Mirzazadeh, N. Schultz, L. Kvastad, A. Andersson, L. Bergenstråhle, J. Bergenstråhle, et al. Spatially resolved clonal copy number alterations in benign and malignant tissue. *Nature*, 608(7922):360–367, 2022.

[37] I. Ezawa, Y. Sawai, T. Kawase, A. Okabe, S. Tsutsumi, H. Ichikawa, Y. Kobayashi, F. Tashiro, H. Namiki, T. Kondo, et al. Novel p53 target gene fuca 1 encodes a fucosidase and regulates growth and survival of cancer cells. *Cancer science*, 107(6):734–745, 2016.

[38] M. T. Flowers and J. M. Ntambi. Role of stearoyl-coenzyme a desaturase in regulating lipid metabolism. *Current opinion in lipidology*, 19(3):248, 2008.

[39] F. Francis, A. Koulakoff, D. Boucher, P. Chafey, B. Schaar, M.-C. Vinet, G. Friocourt, N. McDonnell, O. Reiner, A. Kahn, et al. Doublecortin is a developmentally regulated, microtubule-associated protein expressed in migrating and differentiating neurons. *Neuron*, 23(2):247–256, 1999.

[40] O. Franzén, L.-M. Gan, and J. L. Björkegren. Panglaodb: a web server for exploration of mouse and human single-cell rna sequencing data. *Database*, 2019:baz046, 2019.

[41] B. Fritzsch. *The senses: a comprehensive reference*. Academic Press, 2020.

[42] H. Fu, H. Xu, K. Chong, M. Li, K. S. Ang, H. K. Lee, J. Ling, A. Chen, L. Shao, L. Liu, et al. Unsupervised spatially embedded deep representation of spatial transcriptomics. *Biorxiv*, pages 2021–06, 2021.

[43] T. Fu, L.-J. Dai, S.-Y. Wu, Y. Xiao, D. Ma, Y.-Z. Jiang, and Z.-M. Shao. Spatial architecture of the immune microenvironment orchestrates tumor immunity and therapeutic response. *Journal of hematology & oncology*, 14(1):98, 2021.

[44] B. Gallez. The role of imaging biomarkers to guide pharmacological interventions targeting tumor hypoxia. *Frontiers in pharmacology*, 13:853568, 2022.

[45] J. G. Gleeson, P. T. Lin, L. A. Flanagan, and C. A. Walsh. Doublecortin is a microtubule-associated protein and is expressed widely by migrating neurons. *Neuron*, 23(2):257–271, 1999.

bioRxiv preprint doi: https://doi.org/10.1101/2023.10.10.561757; this version posted October 13, 2023. The copyright holder for this preprint (which was not certified by peer review) is the author/funder, who has granted bioRxiv a license to display the preprint in perpetuity. It is made available under aCC-BY-NC-ND 4.0 International license.

[46] G. Gorin, M. Fang, T. Chari, and L. Pachter. Rna velocity unraveled. *PLOS Computational Biology*, 18(9):e1010492, 2022.

[47] P. Grant, J. Kumar, S. Kar, and M. Overduin. Effects of specific inhibitors for camk1d on a primary neuron model for alzheimer's disease. *Molecules*, 26(24):7669, 2021.

[48] J. Gurdon and P.-Y. Bourillot. Morphogen gradient interpretation. *Nature*, 413(6858):797–803, 2001.

[49] L. Haghverdi, M. Büttner, F. A. Wolf, F. Buettner, and F. J. Theis. Diffusion pseudotime robustly reconstructs lineage branching. *Nature methods*, 13(10):845–848, 2016.

[50] Y. Hao, S. Hao, E. Andersen-Nissen, W. M. M. III, S. Zheng, A. Butler, M. J. Lee, A. J. Wilk, C. Darby, M. Zagar, P. Hoffman, M. Stoeckius, E. Papalexi, E. P. Mimitou, J. Jain, A. Srivastava, T. Stuart, L. B. Fleming, B. Yeung, A. J. Rogers, J. M. McElrath, C. A. Blish, R. Gottardo, P. Smibert, and R. Satija. Integrated analysis of multimodal single-cell data. *Cell*, 2021.

[51] D. Haviv, M. Gatie, A.-K. Hadjantonakis, T. Nawy, and D. Pe'er. The covariance environment defines cellular niches for spatial inference. *bioRxiv*, pages 2023–04, 2023.

[52] S. He, R. Bhatt, B. Birditt, C. Brown, E. Brown, K. Chantranuvatana, P. Danaher, D. Dunaway, B. Filanoski, R. G. Garrison, et al. High-plex multiomic analysis in ffpe tissue at single-cellular and subcellular resolution by spatial molecular imaging. *bioRxiv*, pages 2021–11, 2021.

[53] Y. He, X. Tang, J. Huang, J. Ren, H. Zhou, K. Chen, A. Liu, H. Shi, Z. Lin, Q. Li, et al. Clustermap for multi-scale clustering analysis of spatial gene expression. *Nature communications*, 12(1):5909, 2021.

[54] Y. Hiraoka, O. Komine, M. Nagaoka, N. Bai, K. Hozumi, and K. Tanaka. Delta-like 1 regulates bergmann glial monolayer formation during cerebellar development. *Molecular Brain*, 6:1–12, 2013.

[55] J.-W. Hong, D. A. Hendrix, D. Papatsenko, and M. S. Levine. How the dorsal gradient works: insights from postgenome technologies. *Proceedings of the National Academy of Sciences*, 105(51):20072–20076, 2008.

[56] K. Hornik, M. Stinchcombe, and H. White. Multilayer feedforward networks are universal approximators. *Neural networks*, 2(5):359–366, 1989.

[57] W.-C. Hsieh, B. R. Budiarto, Y.-F. Wang, C.-Y. Lin, M.-C. Gwo, D. K. So, Y.-S. Tzeng, and S.-Y. Chen. Spatial multi-omics analyses of the tumor immune microenvironment. *Journal of Biomedical Science*, 29(1):96, 2022.

[58] J. Hu, X. Li, K. Coleman, A. Schroeder, N. Ma, D. J. Irwin, E. B. Lee, R. T. Shinohara, and M. Li. Spagcn: Integrating gene expression, spatial location and histology to identify spatial domains and spatially variable genes by graph convolutional network. *Nature methods*, 18(11):1342–1351, 2021.

[59] F. Imamura, A. Ito, and B. J. LaFever. Subpopulations of projection neurons in the olfactory bulb. *Frontiers in Neural Circuits*, 14:561822, 2020.

[60] C. Isella, A. Terrasi, S. E. Bellomo, C. Petti, G. Galatola, A. Muratore, A. Mellano, R. Senetta, A. Cassenti, C. Sonetto, et al. Stromal contribution to the colorectal cancer transcriptome. *Nature genetics*, 47(4):312–319, 2015.

bioRxiv preprint doi: https://doi.org/10.1101/2023.10.10.561757; this version posted October 13, 2023. The copyright holder for this preprint (which was not certified by peer review) is the author/funder, who has granted bioRxiv a license to display the preprint in perpetuity. It is made available under aCC-BY-NC-ND 4.0 International license.

[61] A. Janesick, R. Shelansky, A. D. Gottscho, F. Wagner, M. Rouault, G. Beliakoff, M. F. de Oliveira, A. Kohlway, J. Abousoud, C. A. Morrison, et al. High resolution mapping of the breast cancer tumor microenvironment using integrated single cell, spatial and in situ analysis of ffpe tissue. *bioRxiv*, pages 2022–10, 2022.

[62] A. L. Ji, A. J. Rubin, K. Thrane, S. Jiang, D. L. Reynolds, R. M. Meyers, M. G. Guo, B. M. George, A. Mollbrink, J. Bergenstråhle, et al. Multimodal analysis of composition and spatial architecture in human squamous cell carcinoma. *Cell*, 182(2):497–514, 2020.

[63] Q. Jin, J. Zhao, Z. Zhao, S. Zhang, Z. Sun, Y. Shi, H. Yan, Y. Wang, L. Liu, and Z. Zhao. Camk1d inhibits glioma through the pi3k/akt/mtor signaling pathway. *Frontiers in Oncology*, 12:845036, 2022.

[64] A. Jones, F. W. Townes, D. Li, and B. E. Engelhardt. Alignment of spatial genomics data using deep gaussian processes. *Nature Methods*, pages 1–9, 2023.

[65] G. S. Karagiannis, T. Poutahidis, S. E. Erdman, R. Kirsch, R. H. Riddell, and E. P. Diamandis. Cancer-associated fibroblasts drive the progression of metastasis through both paracrine and mechanical pressure on cancer tissue. *Molecular cancer research*, 10(11):1403–1418, 2012.

[66] D. P. Kingma and J. Ba. Adam: A method for stochastic optimization. *arXiv preprint arXiv:1412.6980*, 2014.

[67] D. Klein, G. Palla, M. Lange, M. Klein, Z. Piran, M. Gander, L. Meng-Papaxanthos, M. Sterr, A. Bastidas-Ponce, M. Tarquis-Medina, et al. Mapping cells through time and space with moscot. *bioRxiv*, pages 2023–05, 2023.

[68] O. Komine, M. Nagaoka, K. Watase, D. H. Gutmann, K. Tanigaki, T. Honjo, F. Radtke, T. Saito, S. Chiba, and K. Tanaka. The monolayer formation of bergmann glial cells is regulated by notch/rbp-j signaling. *Developmental biology*, 311(1):238–250, 2007.

[69] V. Kozareva, C. Martin, T. Osorno, S. Rudolph, C. Guo, C. Vanderburg, N. Nadaf, A. Regev, W. G. Regehr, and E. Macosko. A transcriptomic atlas of mouse cerebellar cortex comprehensively defines cell types. *Nature*, 598(7879):214–219, 2021.

[70] G. La Manno, R. Soldatov, A. Zeisel, E. Braun, H. Hochgerner, V. Petukhov, K. Lidschreiber, M. E. Kastriti, P. Lönnerberg, A. Furlan, et al. Rna velocity of single cells. *Nature*, 560(7719):494–498, 2018.

[71] E. S. Lein, M. J. Hawrylycz, N. Ao, M. Ayres, A. Bensinger, A. Bernard, A. F. Boe, M. S. Boguski, K. S. Brockway, E. J. Byrnes, et al. Genome-wide atlas of gene expression in the adult mouse brain. *Nature*, 445(7124):168–176, 2007.

[72] A. W. Leung and J. Y. Li. The molecular pathway regulating bergmann glia and folia generation in the cerebellum. *The Cerebellum*, 17:42–48, 2018.

[73] H. Li, E. T. Courtois, D. Sengupta, Y. Tan, K. H. Chen, J. J. L. Goh, S. L. Kong, C. Chua, L. K. Hon, W. S. Tan, et al. Reference component analysis of single-cell transcriptomes elucidates cellular heterogeneity in human colorectal tumors. *Nature genetics*, 49(5):708–718, 2017.

[74] A. Liberzon, C. Birger, H. Thorvaldsdóttir, M. Ghandi, J. P. Mesirov, and P. Tamayo. The molecular signatures database hallmark gene set collection. *Cell systems*, 1(6):417–425, 2015.

[75] S. L. Lindsay, G. A. McCanney, A. G. Willison, and S. C. Barnett. Multi-target approaches to cns repair: olfactory mucosa-derived cells and heparan sulfates. *Nature Reviews Neurology*, 16(4):229–240, 2020.

bioRxiv preprint doi: https://doi.org/10.1101/2023.10.10.561757; this version posted October 13, 2023. The copyright holder for this preprint (which was not certified by peer review) is the author/funder, who has granted bioRxiv a license to display the preprint in perpetuity. It is made available under aCC-BY-NC-ND 4.0 International license.

[76] W. Liu, X. Liao, Z. Luo, Y. Yang, M. C. Lau, Y. Jiao, X. Shi, W. Zhai, H. Ji, J. Yeong, et al. Probabilistic embedding, clustering, and alignment for integrating spatial transcriptomics data with precast. *Nature communications*, 14(1):296, 2023.

[77] X. Liu, R. Zeira, and B. J. Raphael. Partial alignment of multislice spatially resolved transcriptomics data. *Genome Research*, 2023.

[78] Y. Liu, M. Yang, Y. Deng, G. Su, A. Enninful, C. C. Guo, T. Tebaldi, D. Zhang, D. Kim, Z. Bai, et al. High-spatial-resolution multi-omics sequencing via deterministic barcoding in tissue. *Cell*, 183(6):1665–1681, 2020.

[79] B. Llanas, S. Lantarón, and F. J. Sáinz. Constructive approximation of discontinuous functions by neural networks. *Neural Processing Letters*, 27:209–226, 2008.

[80] P.-M. Lledo and M. Valley. Adult olfactory bulb neurogenesis. *Cold Spring Harbor Perspectives in Biology*, 8(8):a018945, 2016.

[81] Y. Long, K. S. Ang, M. Li, K. L. K. Chong, R. Sethi, C. Zhong, H. Xu, Z. Ong, K. Sachaphibulkij, A. Chen, et al. Spatially informed clustering, integration, and deconvolution of spatial transcriptomics with graphst. *Nature Communications*, 14(1):1155, 2023.

[82] E. Lundberg and G. H. Borner. Spatial proteomics: a powerful discovery tool for cell biology. *Nature Reviews Molecular Cell Biology*, 20(5):285–302, 2019.

[83] C. Ma, U. Chitra, S. Zhang, and B. J. Raphael. Belayer: Modeling discrete and continuous spatial variation in gene expression from spatially resolved transcriptomics. *Cell Systems*, 13(10):786–797, 2022.

[84] S. Mages, N. Moriel, I. Avraham-Davidi, E. Murray, J. Watter, F. Chen, O. Rozenblatt-Rosen, J. Klughammer, A. Regev, and M. Nitzan. Tacco unifies annotation transfer and decomposition of cell identities for single-cell and spatial omics. *Nature Biotechnology*, pages 1–9, 2023.

[85] K. Maher, M. Wu, Y. Zhou, J. Huang, Q. Zhang, and X. Wang. Mitigating autocorrelation during spatially resolved transcriptomics data analysis. *bioRxiv*, pages 2023–06, 2023.

[86] S. A. Mani, W. Guo, M.-J. Liao, E. N. Eaton, A. Ayyanan, A. Y. Zhou, M. Brooks, F. Reinhard, C. C. Zhang, M. Shipitsin, et al. The epithelial-mesenchymal transition generates cells with properties of stem cells. *Cell*, 133(4):704–715, 2008.

[87] J. E. Marsden and A. Tromba. *Vector calculus*. Macmillan, 2003.

[88] V. Marx. Method of the year: spatially resolved transcriptomics. *Nature methods*, 18(1):9–14, 2021.

[89] K. R. Maynard, L. Collado-Torres, L. M. Weber, C. Uytingco, B. K. Barry, S. R. Williams, J. L. Catallini, M. N. Tran, Z. Besich, M. Tippani, et al. Transcriptome-scale spatial gene expression in the human dorsolateral prefrontal cortex. *Nature neuroscience*, 24(3):425–436, 2021.

[90] G.-l. Ming and H. Song. Adult neurogenesis in the mammalian central nervous system. *Annu. Rev. Neurosci.*, 28:223–250, 2005.

[91] J. R. Moffitt, D. Bambah-Mukku, S. W. Eichhorn, E. Vaughn, K. Shekhar, J. D. Perez, N. D. Rubinstein, J. Hao, A. Regev, C. Dulac, et al. Molecular, spatial, and functional single-cell profiling of the hypothalamic preoptic region. *Science*, 362(6416):eaau5324, 2018.

bioRxiv preprint doi: https://doi.org/10.1101/2023.10.10.561757; this version posted October 13, 2023. The copyright holder for this preprint (which was not certified by peer review) is the author/funder, who has granted bioRxiv a license to display the preprint in perpetuity. It is made available under aCC-BY-NC-ND 4.0 International license.

[92] R. Morgan, E. Mortensson, and A. Williams. Targeting lgr5 in colorectal cancer: therapeutic gold or too plastic? *British journal of cancer*, 118(11):1410–1418, 2018.

[93] L. Moses and L. Pachter. Museum of spatial transcriptomics. *Nature Methods*, 19(5):534–546, 2022.

[94] S. Nagayama, R. Homma, and F. Imamura. Neuronal organization of olfactory bulb circuits. *Frontiers in neural circuits*, 8:98, 2014.

[95] A. Nathan, S. Asgari, K. Ishigaki, C. Valencia, T. Amariuta, Y. Luo, J. I. Beynor, Y. Baglaenko, S. Suliman, A. L. Price, et al. Single-cell eqtl models reveal dynamic t cell state dependence of disease loci. *Nature*, 606(7912):120–128, 2022.

[96] L. Ng, A. Bernard, C. Lau, C. C. Overly, H.-W. Dong, C. Kuan, S. Pathak, S. M. Sunkin, C. Dang, J. W. Bohland, et al. An anatomic gene expression atlas of the adult mouse brain. *Nature neuroscience*, 12(3):356–362, 2009.

[97] R. E. Niec, T. Chu, M. Schernthanner, S. Gur-Cohen, L. Hidalgo, H. A. Pasolli, K. A. Luckett, Z. Wang, S. R. Bhalla, F. Cambuli, et al. Lymphatics act as a signaling hub to regulate intestinal stem cell activity. *Cell stem cell*, 29(7):1067–1082, 2022.

[98] R. V. O'Neill, J. Krummel, R. e. a. Gardner, G. Sugihara, B. Jackson, D. DeAngelis, B. Milne, M. G. Turner, B. Zygmunt, S. Christensen, et al. Indices of landscape pattern. *Landscape ecology*, 1:153–162, 1988.

[99] O. Otero-Estévez, M. Martínez-Fernández, L. Vázquez-Iglesias, M. P. de la Cadena, F. J. Rodríguez-Berrocal, and V. S. Martínez-Zorzano. Decreased expression of alpha-l-fucosidase gene fuca1 in human colorectal tumors. *International journal of molecular sciences*, 14(8):16986–16998, 2013.

[100] L. Pachter. Models for transcript quantification from rna-seq. *arXiv preprint arXiv:1104.3889*, 2011.

[101] G. Palla, D. S. Fischer, A. Regev, and F. J. Theis. Spatial components of molecular tissue biology. *Nature Biotechnology*, 40(3):308–318, 2022.

[102] A. Paszke, S. Gross, F. Massa, A. Lerer, J. Bradbury, G. Chanan, T. Killeen, Z. Lin, N. Gimelshein, L. Antiga, et al. Pytorch: An imperative style, high-performance deep learning library. *Advances in neural information processing systems*, 32, 2019.

[103] F. Pedregosa, G. Varoquaux, A. Gramfort, V. Michel, B. Thirion, O. Grisel, M. Blondel, P. Prettenhofer, R. Weiss, V. Dubourg, J. Vanderplas, A. Passos, D. Cournapeau, M. Brucher, M. Perrot, and E. Duchesnay. Scikit-learn: Machine learning in Python. *Journal of Machine Learning Research*, 12:2825–2830, 2011.

[104] D. Pham, X. Tan, J. Xu, L. F. Grice, P. Y. Lam, A. Raghubar, J. Vukovic, M. J. Ruitenberg, and Q. Nguyen. stlearn: integrating spatial location, tissue morphology and gene expression to find cell types, cell-cell interactions and spatial trajectories within undissociated tissues. *BioRxiv*, pages 2020–05, 2020.

[105] J. Piard, J.-H. Hu, P. M. Campeau, S. Rzońca, H. Van Esch, E. Vincent, M. Han, E. Rossignol, J. Castaneda, J. Chelly, et al. Frmpd4 mutations cause x-linked intellectual disability and disrupt dendritic spine morphogenesis. *Human molecular genetics*, 27(4):589–600, 2018.

[106] C. Qi, L. Lei, J. Hu, G. Wang, J. Liu, and S. Ou. Thrombospondin-1 is a prognostic biomarker and is correlated with tumor immune microenvironment in glioblastoma. *Oncology Letters*, 21(1):1–1, 2021.

bioRxiv preprint doi: https://doi.org/10.1101/2023.10.10.561757; this version posted October 13, 2023. The copyright holder for this preprint (which was not certified by peer review) is the author/funder, who has granted bioRxiv a license to display the preprint in perpetuity. It is made available under aCC-BY-NC-ND 4.0 International license.

[107] X. Qiu, Q. Mao, Y. Tang, L. Wang, R. Chawla, H. A. Pliner, and C. Trapnell. Reversed graph embedding resolves complex single-cell trajectories. *Nature methods*, 14(10):979–982, 2017.

[108] X. Qiu, Y. Zhang, J. D. Martin-Rufino, C. Weng, S. Hosseinzadeh, D. Yang, A. N. Pogson, M. Y. Hein, K. H. J. Min, L. Wang, et al. Mapping transcriptomic vector fields of single cells. *Cell*, 185(4):690–711, 2022.

[109] A. Ramón-Cueto and J. Avila. Olfactory ensheathing glia: properties and function. *Brain research bulletin*, 46(3):175–187, 1998.

[110] R. Rangan, S. Khavnekar, A. Lerer, J. Johnston, R. Kelley, M. Obr, A. Kotecha, and E. D. Zhong. Deep reconstructing generative networks for visualizing dynamic biomolecules inside cells. *bioRxiv*, pages 2023–08, 2023.

[111] A. Rao, D. Barkley, G. S. França, and I. Yanai. Exploring tissue architecture using spatial transcriptomics. *Nature*, 596(7871):211–220, 2021.

[112] M. S. B. Raredon, J. Yang, N. Kothapalli, W. Lewis, N. Kaminski, L. E. Niklason, and Y. Kluger. Comprehensive visualization of cell–cell interactions in single-cell and spatial transcriptomics with niches. *Bioinformatics*, 39(1):btac775, 2023.

[113] H. Ren, B. L. Walker, Z. Cang, and Q. Nie. Identifying multicellular spatiotemporal organization of cells with spaceflow. *Nature communications*, 13(1):4076, 2022.

[114] J. Ren, H. Zhou, H. Zeng, C. K. Wang, J. Huang, X. Qiu, X. Sui, Q. Li, X. Wu, Z. Lin, et al. Spatiotemporally resolved transcriptomics reveals the subcellular rna kinetic landscape. *Nature Methods*, pages 1–11, 2023.

[115] M. Revuelta, T. Scheuer, L.-J. Chew, and T. Schmitz. Glial factors regulating white matter development and pathologies of the cerebellum. *Neurochemical Research*, 45:643–655, 2020.

[116] S. G. Rodriques, R. R. Stickels, A. Goeva, C. A. Martin, E. Murray, C. R. Vanderburg, J. Welch, L. M. Chen, F. Chen, and E. Z. Macosko. Slide-seq: A scalable technology for measuring genome-wide expression at high spatial resolution. *Science*, 363(6434):1463–1467, 2019.

[117] K. W. Rogers and A. F. Schier. Morphogen gradients: from generation to interpretation. *Annual review of cell and developmental biology*, 27:377–407, 2011.

[118] A. D. Rouillard, G. W. Gundersen, N. F. Fernandez, Z. Wang, C. D. Monteiro, M. G. McDermott, and A. Ma'ayan. The harmonizome: a collection of processed datasets gathered to serve and mine knowledge about genes and proteins. *Database*, 2016, 2016.

[119] A. J. Russell, J. A. Weir, N. M. Nadaf, M. Shabet, V. Kumar, S. Kambhampati, R. Raichur, G. J. Marrero, S. Liu, K. S. Balderrama, et al. Slide-tags: scalable, single-nucleus barcoding for multi-modal spatial genomics. *bioRxiv*, pages 2023–04, 2023.

[120] A. Sarkar and M. Stephens. Separating measurement and expression models clarifies confusion in single-cell rna sequencing analysis. *Nature genetics*, 53(6):770–777, 2021.

[121] R. Satija, J. A. Farrell, D. Gennert, A. F. Schier, and A. Regev. Spatial reconstruction of single-cell gene expression data. *Nature Biotechnology*, 33:495–502, 2015.

[122] U. Sen, C. Coleman, and T. Sen. Stearoyl coenzyme a desaturase-1: multitasker in cancer, metabolism, and ferroptosis. *Trends in Cancer*, 2023.

bioRxiv preprint doi: https://doi.org/10.1101/2023.10.10.561757; this version posted October 13, 2023. The copyright holder for this preprint (which was not certified by peer review) is the author/funder, who has granted bioRxiv a license to display the preprint in perpetuity. It is made available under aCC-BY-NC-ND 4.0 International license.

[123] T. Serra, C. Tjandraatmadja, and S. Ramalingam. Bounding and counting linear regions of deep neural networks. In *International Conference on Machine Learning*, pages 4558–4566. PMLR, 2018.

[124] E. H. Shen, C. C. Overly, and A. R. Jones. The allen human brain atlas: comprehensive gene expression mapping of the human brain. *Trends in neurosciences*, 35(12):711–714, 2012.

[125] E. A. Smith and H. C. Hodges. The spatial and genomic hierarchy of tumor ecosystems revealed by single-cell technologies. *Trends in cancer*, 5(7):411–425, 2019.

[126] C. Sotelo and F. Rossi. Purkinje cell migration and differentiation. In *Handbook of the cerebellum and cerebellar disorders*, pages 173–205. Springer, 2021.

[127] R. R. Stickels, E. Murray, P. Kumar, J. Li, J. L. Marshall, D. J. Di Bella, P. Arlotta, E. Z. Macosko, and F. Chen. Highly sensitive spatial transcriptomics at near-cellular resolution with slide-seqv2. *Nature biotechnology*, 39(3):313–319, 2021.

[128] I. Straub, L. Witter, A. Eshra, M. Hoidis, N. Byczkowicz, S. Maas, I. Delvendahl, K. Dorgans, E. Savier, I. Bechmann, et al. Gradients in the mammalian cerebellar cortex enable fourier-like transformation and improve storing capacity. *Elife*, 9:e51771, 2020.

[129] K. Street, D. Risso, R. B. Fletcher, D. Das, J. Ngai, N. Yosef, E. Purdom, and S. Dudoit. Slingshot: cell lineage and pseudotime inference for single-cell transcriptomics. *BMC genomics*, 19:1–16, 2018.

[130] S. Sun, J. Zhu, and X. Zhou. Statistical analysis of spatial expression patterns for spatially resolved transcriptomic studies. *Nature methods*, 17(2):193–200, 2020.

[131] X. Sun, X. Liu, E. R. Starr, and S. Liu. Cckergic tufted cells differentially drive two anatomically segregated inhibitory circuits in the mouse olfactory bulb. *Journal of Neuroscience*, 40(32):6189–6206, 2020.

[132] V. Svensson, S. A. Teichmann, and O. Stegle. Spatialde: identification of spatially variable genes. *Nature methods*, 15(5):343–346, 2018.

[133] B. Tepe, M. C. Hill, B. T. Pekarek, P. J. Hunt, T. J. Martin, J. F. Martin, and B. R. Arenkiel. Single-cell rna-seq of mouse olfactory bulb reveals cellular heterogeneity and activity-dependent molecular census of adult-born neurons. *Cell reports*, 25(10):2689–2703, 2018.

[134] L. Tian, F. Chen, and E. Z. Macosko. The expanding vistas of spatial transcriptomics. *Nature Biotechnology*, 41(6):773–782, 2023.

[135] F. W. Townes and B. E. Engelhardt. Nonnegative spatial factorization applied to spatial genomics. *Nature Methods*, 20(2):229–238, 2023.

[136] F. W. Townes, S. C. Hicks, M. J. Aryee, and R. A. Irizarry. Feature selection and dimension reduction for single-cell rna-seq based on a multinomial model. *Genome biology*, 20:1–16, 2019.

[137] C. Trapnell, D. Cacchiarelli, J. Grimsby, P. Pokharel, S. Li, M. Morse, N. J. Lennon, K. J. Livak, T. S. Mikkelsen, and J. L. Rinn. The dynamics and regulators of cell fate decisions are revealed by pseudotemporal ordering of single cells. *Nature biotechnology*, 32(4):381–386, 2014.

[138] S. van Vliet, A. R. Winkler, S. Spriewald, B. Stecher, M. Ackermann, et al. Spatially correlated gene expression in bacterial groups: the role of lineage history, spatial gradients, and cell-cell interactions. *Cell systems*, 6(4):496–507, 2018.

bioRxiv preprint doi: https://doi.org/10.1101/2023.10.10.561757; this version posted October 13, 2023. The copyright holder for this preprint (which was not certified by peer review) is the author/funder, who has granted bioRxiv a license to display the preprint in perpetuity. It is made available under aCC-BY-NC-ND 4.0 International license.

[139] B. Velten and O. Stegle. Principles and challenges of modeling temporal and spatial omics data. *Nature Methods*, pages 1–13, 2023.

[140] J. Voogd and M. Glickstein. The anatomy of the cerebellum. *Trends in cognitive sciences*, 2(9):307–313, 1998.

[141] L. Wang, X. Xing, X. Zeng, S. R. Jackson, T. TeSlaa, O. Al-Dalahmah, L. Z. Samarah, K. Goodwin, L. Yang, M. R. McReynolds, et al. Spatially resolved isotope tracing reveals tissue metabolic activity. *Nature methods*, 19(2):223–230, 2022.

[142] S. Wang, T. Ye, G. Li, X. Zhang, and H. Shi. Margination and adhesion dynamics of tumor cells in a real microvascular network. *PLoS Computational Biology*, 17(2):e1008746, 2021.

[143] X. Wang, W. E. Allen, M. A. Wright, E. L. Sylwestrak, N. Samusik, S. Vesuna, K. Evans, C. Liu, C. Ramakrishnan, J. Liu, et al. Three-dimensional intact-tissue sequencing of single-cell transcriptional states. *Science*, 361(6400):eaat5691, 2018.

[144] S. A. Watson and G. P. McStay. Functions of cytochrome c oxidase assembly factors. *International Journal of Molecular Sciences*, 21(19):7254, 2020.

[145] L. M. Weber, A. Saha, A. Datta, K. D. Hansen, and S. C. Hicks. nnsvg for the scalable identification of spatially variable genes using nearest-neighbor gaussian processes. *Nature communications*, 14(1):4059, 2023.

[146] L. Wernecke, S. Keckeis, N. Reichhart, O. Strauß, and D. J. Salchow. Epithelial-mesenchymal transdifferentiation in pediatric lens epithelial cells. *Investigative ophthalmology & visual science*, 59(15):5785–5794, 2018.

[147] S. S. Wilks. The large-sample distribution of the likelihood ratio for testing composite hypotheses. *The annals of mathematical statistics*, 9(1):60–62, 1938.

[148] P. A. Wilson and D. A. Melton. Mesodermal patterning by an inducer gradient depends on secondary cell–cell communication. *Current Biology*, 4(8):676–686, 1994.

[149] Y. Wu, S. Yang, J. Ma, Z. Chen, G. Song, D. Rao, Y. Cheng, S. Huang, Y. Liu, S. Jiang, et al. Spatiotemporal immune landscape of colorectal cancer liver metastasis at single-cell level. *Cancer discovery*, 12(1):134–153, 2022.

[150] Z. Wu, A. E. Trevino, E. Wu, K. Swanson, H. J. Kim, H. B. D'Angio, R. Preska, G. W. Charville, P. D. Dalerba, A. M. Egloff, et al. Graph deep learning for the characterization of tumour microenvironments from spatial protein profiles in tissue specimens. *Nature Biomedical Engineering*, 6(12):1435–1448, 2022.

[151] H. Xie and M. C. Simon. Oxygen availability and metabolic reprogramming in cancer. *Journal of Biological Chemistry*, 292(41):16825–16832, 2017.

[152] Y. Xie, T. Takikawa, S. Saito, O. Litany, S. Yan, N. Khan, F. Tombari, J. Tompkin, V. Sitzmann, and S. Sridhar. Neural fields in visual computing and beyond (2021), 2021.

[153] C. Xu, X. Jin, S. Wei, P. Wang, M. Luo, Z. Xu, W. Yang, Y. Cai, L. Xiao, X. Lin, et al. Deepst: identifying spatial domains in spatial transcriptomics by deep learning. *Nucleic Acids Research*, 50(22):e131–e131, 2022.

bioRxiv preprint doi: https://doi.org/10.1101/2023.10.10.561757; this version posted October 13, 2023. The copyright holder for this preprint (which was not certified by peer review) is the author/funder, who has granted bioRxiv a license to display the preprint in perpetuity. It is made available under aCC-BY-NC-ND 4.0 International license.

[154] C. Xu, R. Lopez, E. Mehlman, J. Regier, M. I. Jordan, and N. Yosef. Probabilistic harmonization and annotation of single-cell transcriptomics data with deep generative models. *Molecular systems biology*, 17(1):e9620, 2021.

[155] Y. Yang, A. H. Kim, and A. Bonni. The dynamic ubiquitin ligase duo: Cdh1-apc and cdc20-apc regulate neuronal morphogenesis and connectivity. *Current opinion in neurobiology*, 20(1):92–99, 2010.

[156] Y. Yu, D. Liu, Z. Liu, S. Li, Y. Ge, W. Sun, and B. Liu. The inhibitory effects of col1a2 on colorectal cancer cell proliferation, migration, and invasion. *Journal of Cancer*, 9(16):2953, 2018.

[157] Y. Yuan. Spatial heterogeneity in the tumor microenvironment. *Cold Spring Harbor perspectives in medicine*, 6(8), 2016.

[158] M. Zaidi, F. Fu, D. Cojocari, T. D. McKee, and B. G. Wouters. Quantitative visualization of hypoxia and proliferation gradients within histological tissue sections. *Frontiers in Bioengineering and Biotechnology*, 7:397, 2019.

[159] R. Zeira, M. Land, A. Strzalkowski, and B. J. Raphael. Alignment and integration of spatial transcriptomics data. *Nature Methods*, 19(5):567–575, 2022.

[160] H. Zeng. What is a cell type and how to define it? *Cell*, 185(15):2739–2755, 2022.

[161] H. Zeng, J. Huang, J. Ren, C. K. Wang, Z. Tang, H. Zhou, Y. Zhou, H. Shi, A. Aditham, X. Sui, et al. Spatially resolved single-cell translatomics at molecular resolution. *Science*, 380(6652):eadd3067, 2023.

[162] H. Zeng, J. Huang, H. Zhou, W. J. Meilandt, B. Dejanovic, Y. Zhou, C. J. Bohlen, S.-H. Lee, J. Ren, A. Liu, et al. Integrative in situ mapping of single-cell transcriptional states and tissue histopathology in a mouse model of alzheimer's disease. *Nature Neuroscience*, 26(3):430–446, 2023.

[163] S. Zeppilli, T. Ackels, R. Attey, N. Klimpert, K. D. Ritola, S. Boeing, A. Crombach, A. T. Schaefer, and A. Fleischmann. Molecular characterization of projection neuron subtypes in the mouse olfactory bulb. *Elife*, 10:e65445, 2021.

[164] D. Zhang, Y. Deng, P. Kukanja, E. Agirre, M. Bartosovic, M. Dong, C. Ma, S. Ma, G. Su, S. Bao, et al. Spatial epigenome–transcriptome co-profiling of mammalian tissues. *Nature*, 616(7955):113–122, 2023.

[165] H. Zhang, H. Lu, L. Xiang, J. W. Bullen, C. Zhang, D. Samanta, D. M. Gilkes, J. He, and G. L. Semenza. Hif-1 regulates cd47 expression in breast cancer cells to promote evasion of phagocytosis and maintenance of cancer stem cells. *Proceedings of the National Academy of Sciences*, 112(45):E6215–E6223, 2015.

[166] X. Zhang, T. Huang, Y. Li, and H. Qiu. Upregulation of thbs1 is related to immunity and chemotherapy resistance in gastric cancer. *International journal of general medicine*, pages 4945–4957, 2021.

[167] X. Zhang, X. Wang, G. Shivashankar, and C. Uhler. Graph-based autoencoder integrates spatial transcriptomics with chromatin images and identifies joint biomarkers for alzheimer's disease. *Nature Communications*, 13(1):7480, 2022.

[168] E. Zhao, M. R. Stone, X. Ren, J. Guenthoer, K. S. Smythe, T. Pulliam, S. R. Williams, C. R. Uytingco, S. E. Taylor, P. Nghiem, et al. Spatial transcriptomics at subspot resolution with bayesspace. *Nature biotechnology*, 39(11):1375–1384, 2021.

bioRxiv preprint doi: https://doi.org/10.1101/2023.10.10.561757; this version posted October 13, 2023. The copyright holder for this preprint (which was not certified by peer review) is the author/funder, who has granted bioRxiv a license to display the preprint in perpetuity. It is made available under aCC-BY-NC-ND 4.0 International license.

[169] J. Zheng. Energy metabolism of cancer: Glycolysis versus oxidative phosphorylation. *Oncology letters*, 4(6):1151–1157, 2012.

[170] Q. Zhou, J. Qin, Y. Liang, W. Zhang, S. He, F. Tissir, Y. Qu, and L. Zhou. Celsr3 is required for purkinje cell maturation and regulates cerebellar postsynaptic plasticity. *Iscience*, 24(7):102812, 2021.

[171] J. Zhu, S. Sun, and X. Zhou. Spark-x: non-parametric modeling enables scalable and robust detection of spatial expression patterns for large spatial transcriptomic studies. *Genome biology*, 22(1):1–25, 2021.

bioRxiv preprint doi: https://doi.org/10.1101/2023.10.10.561757; this version posted October 13, 2023. The copyright holder for this preprint (which was not certified by peer review) is the author/funder, who has granted bioRxiv a license to display the preprint in perpetuity. It is made available under aCC-BY-NC-ND 4.0 International license.

Supplemental Information

A Expression models and pooling

We assume the UMI counts $a_{i,g}$ follow the Poisson expression model, i.e. the UMI counts $a_{i,g}$ are independent and follow a Poisson distribution of the form $a_{i,g} \overset{\text{i.i.d.}}{\sim} \text{Pois}\Big(U_i \cdot \exp\big(f_g(x_i, y_i)\big)\Big)$ where U_i is the total UMI count at spot i.

Suppose the isodepth d is known, and let $\gamma_1, \ldots, \gamma_{N'}$ be the unique isodepth values $d(x_i, y_i)$ across all spots $\mathbf{s}_i = (x_i, y_i)$. Let $B_j = \{i : d(x_i, y_i) = \gamma_j\}$ be the set of spots with isodepth equal to γ_j. Let $\widetilde{a}_{j,g} = \sum_{i \in B_j} a_{i,g}$ be the total expression for gene g over all spots $i \in B_j$, i.e. $\widetilde{a}_{j,g}$ is the total expression for all spots with isodepth γ_j. We say B_j is a *pooled* spot and we call $\widetilde{a}_{j,g}$ the *pooled* expression of gene g at the j-th pooled spot.

The solution to the MLE problem in (9) with isodepth d is equal to the solution of the following optimization problem

$$\underset{\substack{b_1 < b_2 < \cdots < b_{P-1} \\ \mathbf{h} = (h_1, \ldots, h_G) \in \mathcal{L}(b_1, \ldots, b_{P-1})}}{\operatorname{argmax}} \quad \sum_{g=1}^{G} \left(\sum_{j=1}^{N'} \log \mathbb{P}\Big(\widetilde{a}_{j,g} \mid h_g\big(d(x_j, y_j)\big)\Big) \right) \tag{20}$$

where the inference is performed with pooled expression values $\widetilde{a}_{j,g}$. Thus, one obtains the same expression function $\mathbf{h}$ whether one computes the MLE (9) over all data points, or first sums spots with the same isodepth, i.e. *pooling* spots by their isodepth, and then computes the MLE. See [83] for more details.

B Dimensionality reduction using GLM-PCA

Given SRT data $(\mathbf{A}, \mathbf{S})$, we first run GLM-PCA (generalized linear model principal components analysis) [136] and obtain the top-$2P$ GLM-PCs $\mathbf{u}_j = [u_{i,j}] \in \mathbb{R}^N$ for $j = 1, \ldots, 2P$. Next, we compute the MLE in (9) using these PCs and a Gaussian error model, i.e. we solve

$$\underset{\substack{d \in C(\mathbb{R}^2, \mathbb{R}) \\ b_1 < b_2 < \cdots < b_{P-1} \\ \mathbf{h}' = (h'_1, \ldots, h'_{2P}) \in \mathcal{L}(b_1, \ldots, b_{P-1})}}{\operatorname{argmax}} \quad \sum_{j=1}^{2P} \left(\sum_{i=1}^{N} \log \mathbb{P}\Big(u_{i,j} \mid h'_j\big(d(x_i, y_i)\big)\Big) \right) \tag{21}$$

with $u_{i,j} \overset{\text{i.i.d.}}{\sim} N\Big(h'_g\big(d(x_i, y_i)\big), \sigma^2\Big)$ for some shared variance parameter σ^2. (Note that the value of the variance σ^2 does not affect the solution to (21).) Solving (21) an estimated isodepth $\widehat{d}$ and breakpoints $\widehat{b}_1, \cdots, \widehat{b}_{P-1}$.

Finally, we solve the MLE problem in (9) fixing the estimated isodepth $\widehat{d}$ and breakpoints $\widehat{b}_1, \ldots, \widehat{b}_{P-1}$, i.e.

$$\underset{\mathbf{h} = (h_1, \ldots, h_G) \in \mathcal{L}(\widehat{b}_1, \ldots, \widehat{b}_{P-1})}{\operatorname{argmax}} \quad \sum_{g=1}^{G} \left(\sum_{i=1}^{N} \log \mathbb{P}\Big(a_{i,g} \mid h_g\big(\widehat{d}(x_i, y_i)\big)\Big) \right), \tag{22}$$

where we assume the UMI counts $a_{i,g}$ follow the Poisson expression model described above. Solving (22) is equivalent to solving $G \cdot P$ Poisson regression problems, one problem for each combination of the G genes and P spatial clusters.

bioRxiv preprint doi: https://doi.org/10.1101/2023.10.10.561757; this version posted October 13, 2023. The copyright holder for this preprint (which was not certified by peer review) is the author/funder, who has granted bioRxiv a license to display the preprint in perpetuity. It is made available under aCC-BY-NC-ND 4.0 International license.

C Comparison to SpaceFlow

SpaceFlow [113] learns a 1-D coordinate, which they call a *pseudo-Spatialtemporal Map (pSM)*, at each spatial location in a tissue by running diffusion pseudotime [49] on embeddings obtained from a graph neural network. We compared the SpaceFlow pSM to the GASTON isodepth on the mouse cerebellum SRT data from Section 2.2 (Figure S1A,B) and the mouse olfactory bulb SRT data from Section 2.5 (Figure S6C,D). Visually, the isodepth learned by GASTON varies continuously in the tissue while the SpaceFlow pSM does not. For example, in the cerebellum, the pSM is constant — and thus does not continuously vary — within each spatial domain, e.g. in the granule layer, the contours of the isodepth (Figure S1C) smoothly vary while the contours of the pSM (Figure S1D) are irregular. In the olfactory bulb, the pSM is constant in the interior of the tissue (Figure S6C).

We quantify the continuous variation within each layer using the quartile coefficient of dispersion (QCOD) [15], a robust statistic measuring the variation of a dataset, with a large QCOD indicating a larger degree of variation in the data. We first scale the isodepth and the pSM to be in $[0, 1]$ so that they have the same measurement scale; moreover, before computing the QCOD within each layer, we shift the measurements to have the same mean in order to guarantee that the QCOD values are comparable. We observe that in the cerebellum, GASTON has larger QCOD than SpaceFlow in three out of four spatial domains (Figure S1E), indicating that there is substantially more spatial variation in the GASTON isodepth compared to the SpaceFlow pSM. Similarly, in the olfactory bulb, GASTON has larger QCOD than SpaceFlow in six out of seven domains (Figure S6B).

D DLPFC comparison

We evaluated GASTON on SRT data from the human dorsolateral prefrontal cortex (DLPFC) measured with 10x Visium [89]. We analyzed eight DLPFC tissue slices from two donors. These slices were manually annotated with the six layers of the DLPFC and white matter (WM) and have a curved, layered geometry, providing spatial structure that may help GASTON accurately learn the geometry of these tissue slices. We compared the spatial domains identified by GASTON to two graph deep learning approaches, SpaGCN [58] and STAGATE, and our previous method Belayer [83], which requires supervision in the form of approximate layer boundaries. We evaluated each method by computing the adjusted Rand index (ARI) between the estimated spatial domains and the manually annotated layers.

GASTON achieves a higher average AUPRC than the graph deep learning methods SpaGCN and STAGATE (Figure S3A). Moreover, despite being completely unsupervised, GASTON has comparable AUPRC to Belayer, which requires supervision (Figure S3A,B). Importantly, the isodepth $d(x, y)$ learned by GASTON (Figure S3C) is highly correlated with the "relative depth" $\widetilde{d}(x, y)$ that Belayer estimates by solving the heat equation with known layer boundaries (Figure S3D), demonstrating that the neural network used by GASTON indeed learns the cortical depth of each layer. On the other hand, the isodepth d has lower correlation (Figure S3D) with both the top principal component (PC1) and the top generalized linear model principal component (GLM-PC1), which are derived solely from gene expression and do not use the spatial coordinates. These comparisons indicate the importance of spatial information in deriving an accurate measurement of layer depth.

Overall, the improved performance of GASTON demonstrates the value of using simple and interpretable neural network architectures.

bioRxiv preprint doi: https://doi.org/10.1101/2023.10.10.561757; this version posted October 13, 2023. The copyright holder for this preprint (which was not certified by peer review) is the author/funder, who has granted bioRxiv a license to display the preprint in perpetuity. It is made available under aCC-BY-NC-ND 4.0 International license.

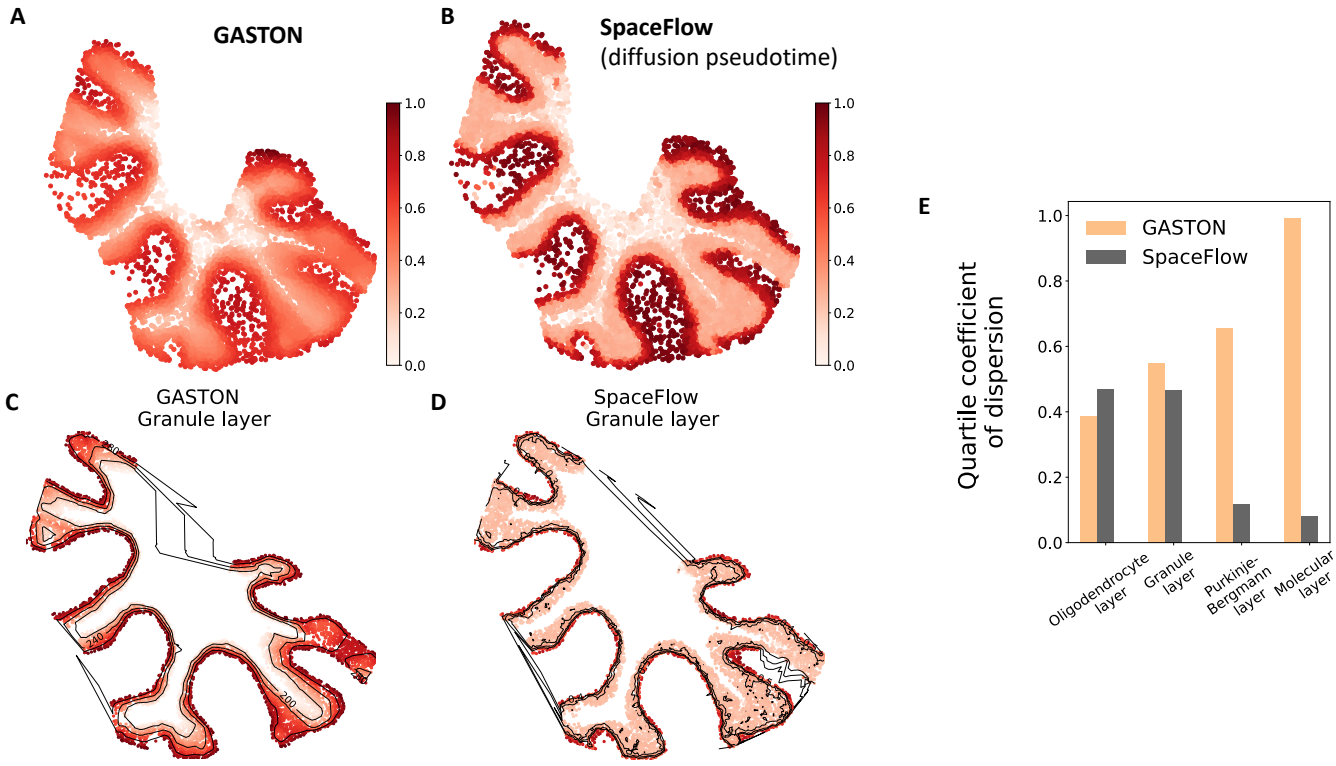

Figure S1: **(A)** The isodepth $d(x, y)$ learned by GASTON scaled to $[0, 1]$. **(B)** The pseudo-Spatiotemporal Map (pSM) learned by SpaceFlow [113] scaled to $[0, 1]$. **(C)** The isodepth $d(x, y)$ in the granule layer (as identified by GASTON), shown with three equally spaced contours of equal isodepth. **(D)** The pSM in the granule layer shown with three equally spaced contours of equal pSM. **(E)** The quartile coefficient of dispersion of the GASTON isodepth and the SpaceFlow pSM in each layer of the cerebellum.

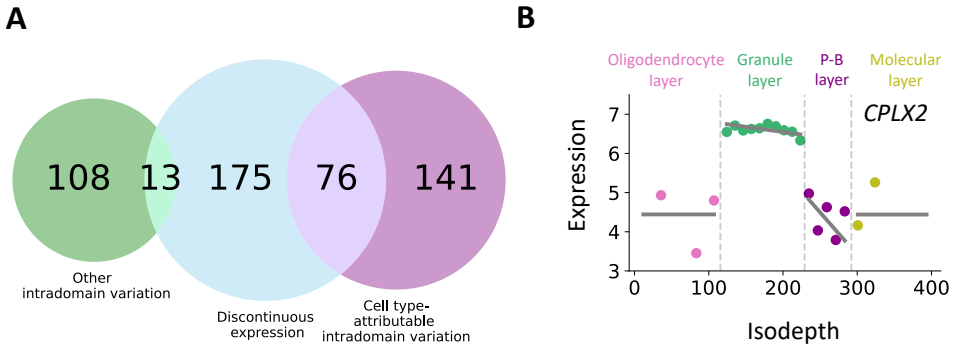

Figure S2: **(A)** Venn diagram of spatially varying genes identified by GASTON in the mouse cerebellum. Numbers indicate genes with specified spatial expression pattern(s). **(B)** Isodepth versus expression for *CPLX2*, which has discontinuities in expression at the granule layer boundaries.

bioRxiv preprint doi: https://doi.org/10.1101/2023.10.10.561757; this version posted October 13, 2023. The copyright holder for this preprint (which was not certified by peer review) is the author/funder, who has granted bioRxiv a license to display the preprint in perpetuity. It is made available under aCC-BY-NC-ND 4.0 International license.

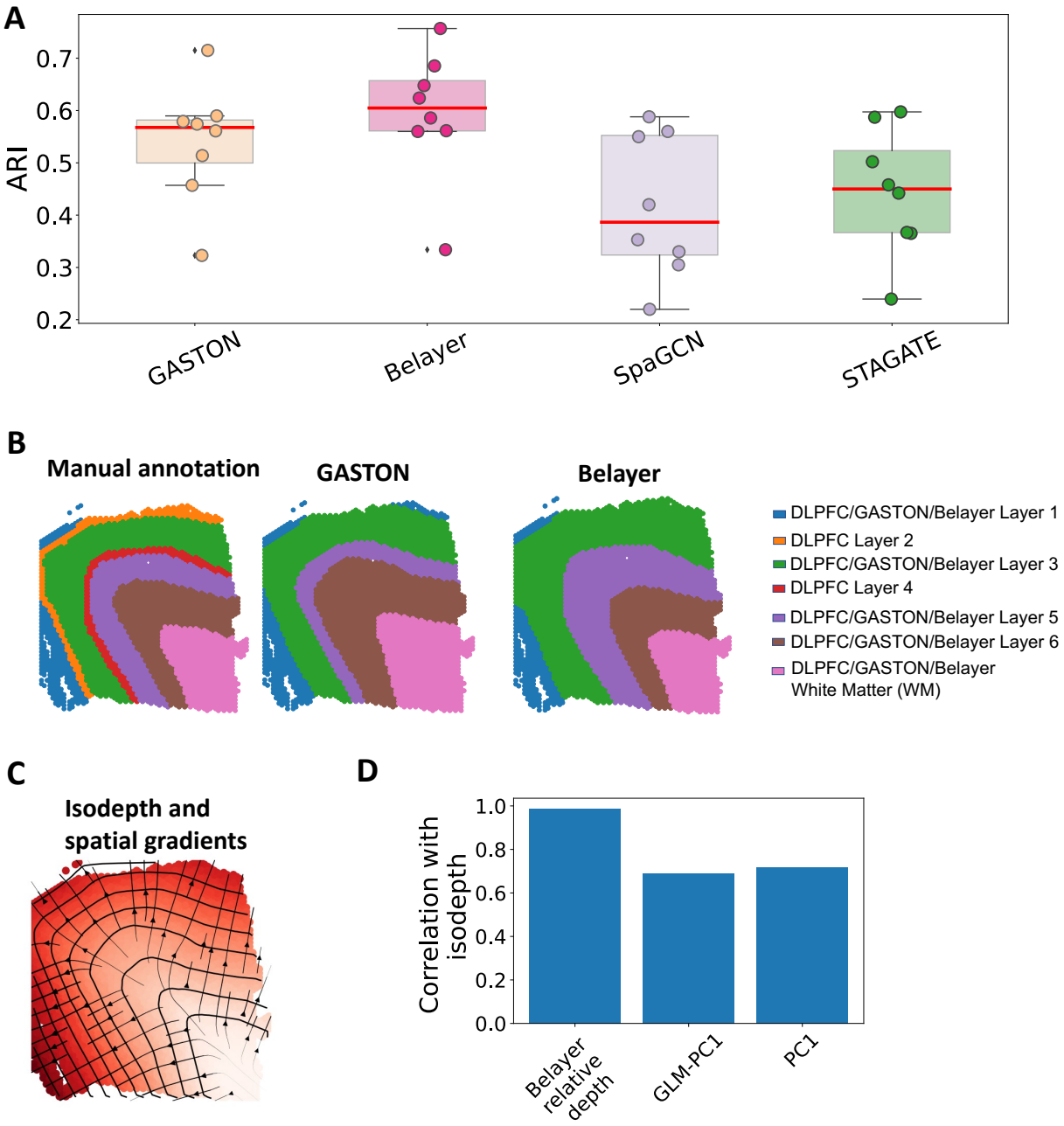

Figure S3: **(A)** Adjusted rand index (ARI) for GASTON, Belayer [83], SpaGCN [58], and STAGATE [32] in identifying the spatial domains of the dorsolateral prefrontal cortex (DLPFC). **(B)** The manually annotated domains and the domains identified by GASTON and Belayer for DLPFC sample 151673. **(C)** Isodepth d and spatial gradients ∇d learned by GASTON for DLPFC sample 151673. **(D)** Correlation between the GASTON isodepth d and (1) the relative depth $\widetilde{d}$ estimated by Belayer using prior knowledge of the layer boundaries (Belayer relative depth); (2) the first generalized linear model principal component (GLM-PC1); and (3) the first principal component (PC1).

bioRxiv preprint doi: https://doi.org/10.1101/2023.10.10.561757; this version posted October 13, 2023. The copyright holder for this preprint (which was not certified by peer review) is the author/funder, who has granted bioRxiv a license to display the preprint in perpetuity. It is made available under aCC-BY-NC-ND 4.0 International license.

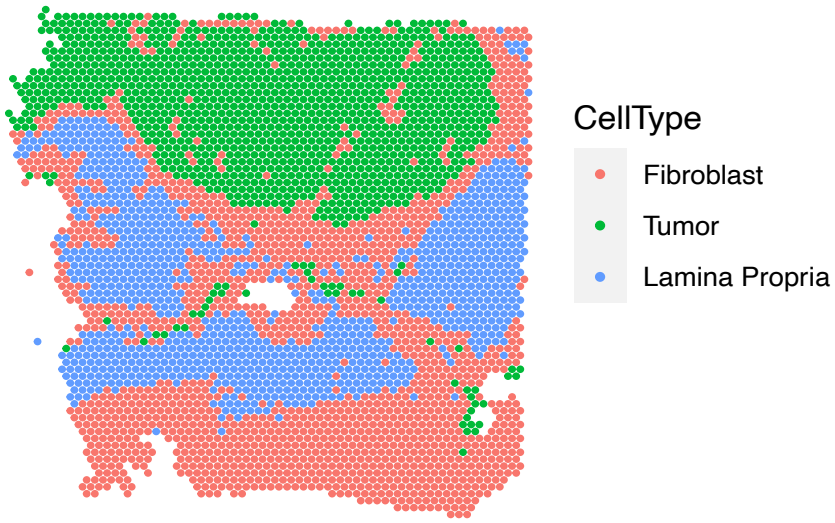

Figure S4: Cell type labels for each spot in 10x Genomics Visium data from a colorectal tumor slice derived in the original study [149] using Seurat [17].

bioRxiv preprint doi: https://doi.org/10.1101/2023.10.10.561757; this version posted October 13, 2023. The copyright holder for this preprint (which was not certified by peer review) is the author/funder, who has granted bioRxiv a license to display the preprint in perpetuity. It is made available under aCC-BY-NC-ND 4.0 International license.

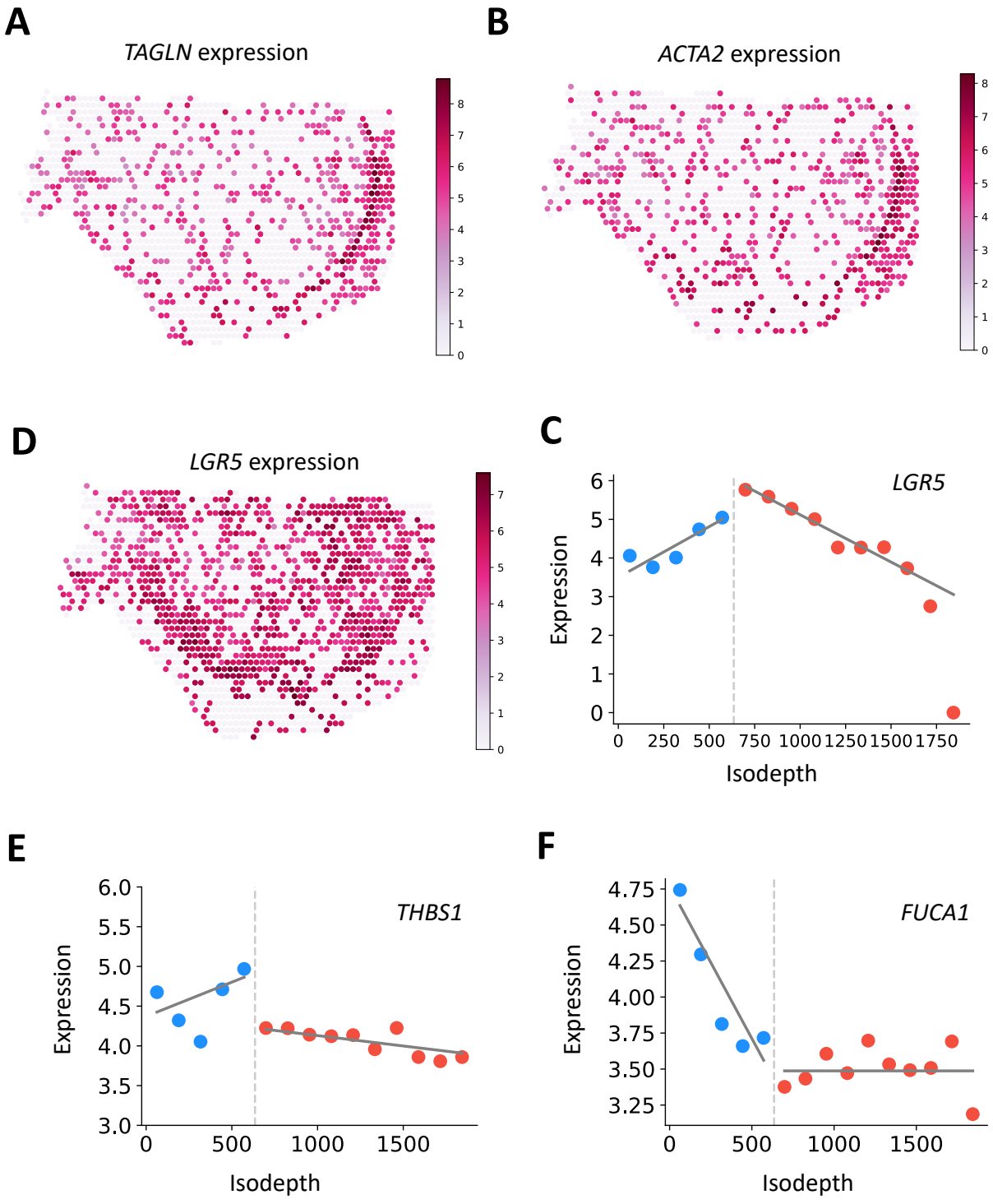

Figure S5: **(A-C)** Expression shown in log CPM for Type II genes **(A)** *TAGLN*, **(B)** *ACTA2*, and **(C)** *LGR5*. **(D-F)** Expression versus isodepth for Type II gene **(D)** *LGR5* and Type III genes **(E)** *THBS1* and **(F)** *FUCA1*.

bioRxiv preprint doi: https://doi.org/10.1101/2023.10.10.561757; this version posted October 13, 2023. The copyright holder for this preprint (which was not certified by peer review) is the author/funder, who has granted bioRxiv a license to display the preprint in perpetuity. It is made available under aCC-BY-NC-ND 4.0 International license.

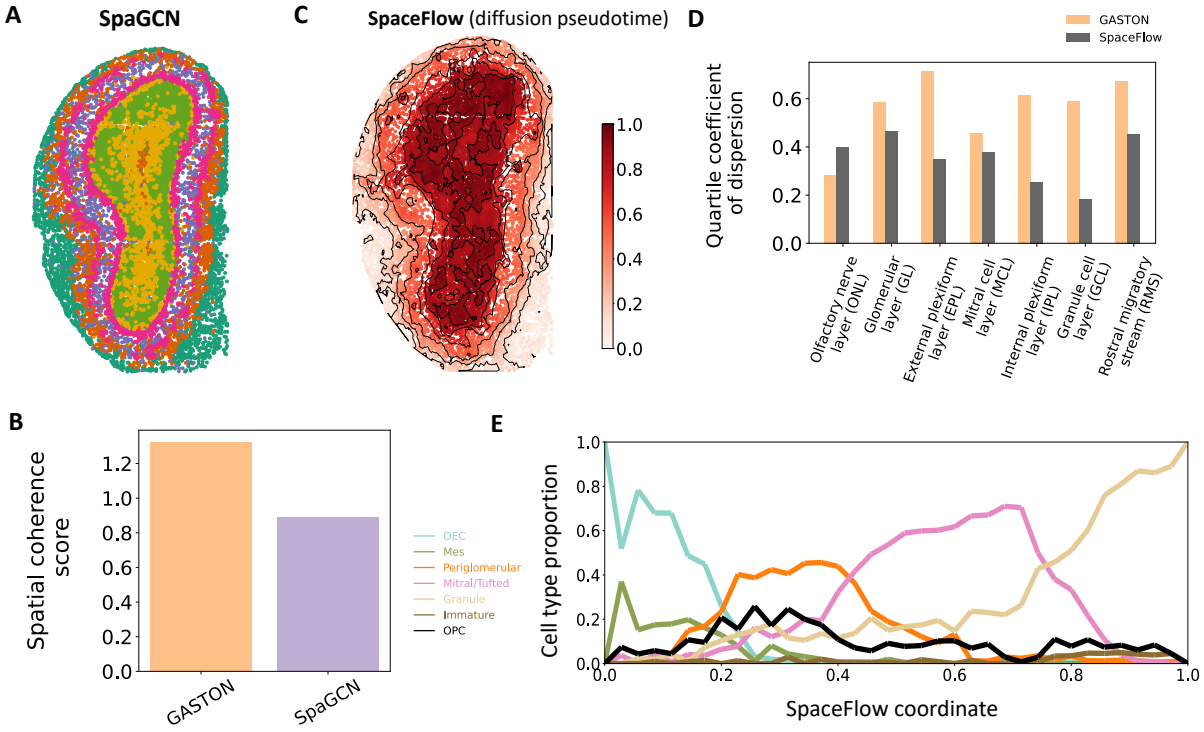

Figure S6: **(A)** Spatial domains learned by SpaGCN [58]. **(B)** Spatial coherence of spatial domains identified by GASTON (Figure 5C) and SpaGCN. **(C)** Pseudospatial-temporal map (pSM) learned by SpaceFlow [113], which utilizes the scRNA-seq based method diffusion pseudotime [49]. Curves denote contour lines of equal pSM. **(D)** Quartile coefficient of dispersion of the GASTON isodepth and the SpaceFlow pSM in each spatial domain identified by GASTON. **(E)** Cell type proportion as a function of SpaceFlow pSM.

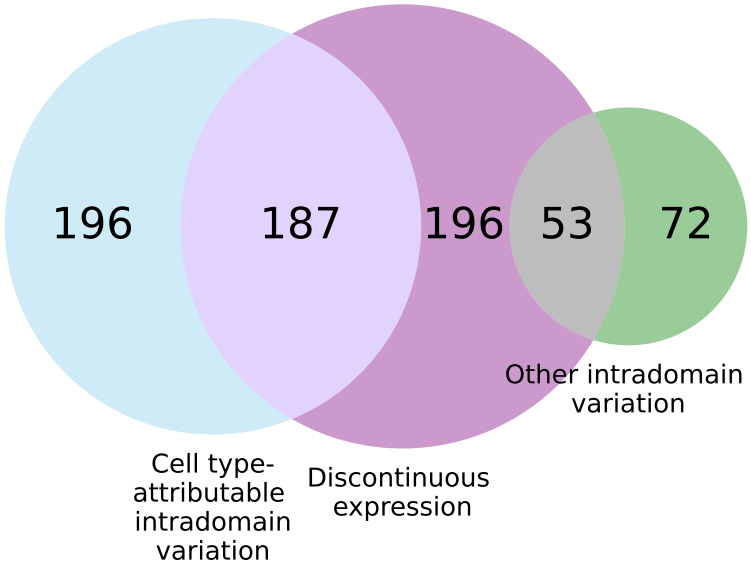

Figure S7: Venn diagram of spatially varying genes identified by GASTON in the olfactory bulb.